DESIGN AND CONTROL OF A MAGNETIC HAMMER MILLIROBOT FOR TISSUE PENETRATION

A Thesis

Presented to

the Faculty of the Department of Mechanical Engineering

University of Houston

in Partial Fulfillment

of the Requirements for the Degree

Master of Science

in Mechanical Engineering

by

Ashwin V. Ramakrishnan

May 2017

DESIGN AND CONTROL OF A MAGNETIC HAMMER MILLIROBOT FOR TISSUE PENETRATION

Ashwin V. Ramakrishnan

Approved:

Chair of the Committee
Karolos Grigoriadis, Professor
Department of Mechanical Engineering

Committee Members:

Aaron T. Becker, Assistant Professor
Department of Electrical and Computer Engineering

Yi Chao Chen, Professor
Department of Mechanical Engineering

Nikolaos V. Tsekos, Associate Professor
Department of Computer Science

Suresh K. Khator, Associate Dean,
Cullen College of Engineering

Pradeep Sharma, Professor and Chair,
Mechanical Engineering

Acknowledgements

This project was made possible thanks to many wonderful people. I am immensely grateful to my adviser, Dr. Aaron T. Becker, for his guidance, and pushing me to produce results while enjoying the process of research. Many thanks to Dr. Julien Leclerc, post-doctoral researcher at the Robotic Swarm Control Lab, for his assistance and patient guidance through the length of this project. I am immensely grateful and thankful to Dusty O'Day for being an indirect mentor, a great friend, and putting me in touch with the right people at the right time. Thanks to Javier Garcia and Jarrett Lonsford for their help with the experiments. Also, thanks to everyone at the Robotic Swarm Control Lab for always providing a helping hand. Last but never the least, much love to my parents and Divya for their unwavering support over the last couple of years.

Also, this work was made possible thanks to funding from the National Science Foundation, grant numbers 1646566 and 1553063.

DESIGN AND CONTROL OF A MAGNETIC HAMMER MILLIROBOT FOR TISSUE PENETRATION

An Abstract

of a

Thesis

Presented to

the Faculty of the Department of Mechanical Engineering

University of Houston

in Partial Fulfillment

of the Requirements for the Degree

Master of Science

in Mechanical Engineering

by

Ashwin V. Ramakrishnan

May 2017

Abstract

Millirobots propelled by magnetic fields show promise for minimally invasive surgery or drug delivery. MRI scanners can generate magnetic gradients to apply propulsive forces on ferromagnetic objects. However, MRI gradient forces are insufficient for tissue penetration. This project presents a millirobot design and control methods to produce pulsed forces. A ferromagnetic sphere inside a hollow robot body can move back and forth between a spring and an impact rod. Repeated impacts convert the kinetic energy of the sphere into large pulsed forces that can penetrate tissue. An estimator helps achieve the maximum possible average impact velocity with minimal sensing, for a given set of material and geometric parameters, and input magnetic gradient force. Prototypes were 3D printed and tested on a custom magnetic test bed. Analytical, numerical and experimental results are presented.

Table of Contents

List of Figures

List of Tables

Chapter 1

Introduction

Minimally invasive surgery (MIS) is a rapidly advancing field in medical treatment. The main advantage being that recovery times are much shorter for patients. Although catheters and endoscopes are currently the most widely used MIS tools, wireless control of miniature, untethered robots through passageways in human bodies is being seen as the next rung on the technological ladder [1, 2, 3]. These methods could provide advantages over current MIS methods such as preventing tissue damage by tethers and reducing chances of blood vessel blockage, especially for complex pathways [4]. Untethered navigation can be achieved by placing a ferromagnetic piece inside the robot and producing a controlled magnetic field around a patient. Propulsion and steering of millirobots can be accomplished by either moving a permanent magnet assembly around a patient [5] or by controlling the current inside electromagnets [6]. The latter solution is often realized with an MRI scanner which already includes electromagnets. In an MRI, the background field magnetizes the ferrous components of the robot, and the gradient coils generate the magnetic gradient necessary to produce forces. The MRI scanner can be used simultaneously to provide real-time imaging of the operating area as well as positioning of the robot.

The force generated on the millirobots is proportional to the field gradient strength. Commercial MRI scanners produce gradients in the range of 20 to 40 mT/m. These gradients are sufficient to maneuver milli-robots inside fluid-filled regions of the body, such as vessels [7], but insufficient for tissue penetration that requires larger forces [8]. Tissue penetration is required for many procedures, including brachytherapy and micro-biopsy. This paper presents a control method, denoted

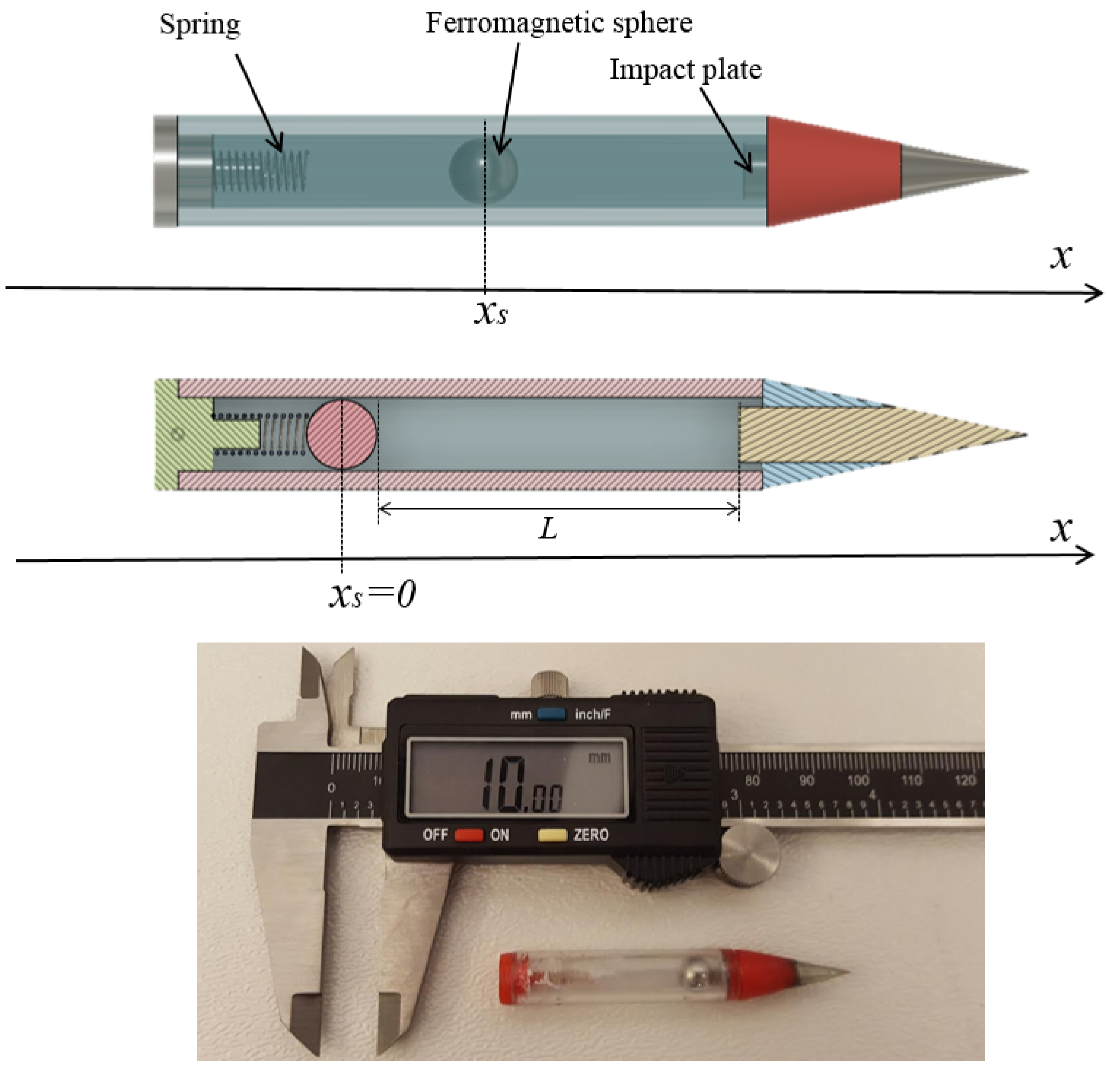

Figure 1.1: Design and prototype of the magnetic hammer millirobot

magnetic hammer actuation, that can generate large pulsed forces for tissue penetration. As in 1.1, the millirobot has a tubular structure in which a ferromagnetic sphere can move back and forth.

This movement is produced by alternately changing the gradient direction. On the posterior side of the millirobot, a spring allows the sphere to change direction smoothly. On the anterior side, a hard rod creates a surface for the sphere to impact, the *impact rod*. Repeated impacts result in large pulsed forces that enable progressive tissue penetration. Simulations and experimental results of three different control methods are also discussed, where each method varies the frequency and duty cycle of the magnetic gradient force input. The three methods are discussed as open-loop, partially closed-loop and ideally closed-loop systems. In the open-loop system, there is no sensing and the magnetic gradient force is switched based on an arbitrary constant frequency. For the partially closed-loop system, the impact of the sphere at the anterior end is sensed using a sensor. This is used to switch the direction of the magnetic gradient force at the impact end. The switching time at the posterior end is set manually and swept through a range of values. Finally for a fully-closed loop system, sensing is used at both ends to switch the direction of the magnetic gradient force such that it is always aligned with the direction of sphere motion. An in-house magnetic test bench has then been used to test these different control strategies and demonstrate tissue penetration. The test setup includes coils, sensors, power electronics, and a real-time controller.

The first part of the following chapter reviews literature about magnetic actuation of particles or objects for minimally invasive applications. The second part of the literature review covers forces involved in tissue penetration by needle insertion. The third chapter explains the millirobot design, the underlying mechanical and magnetic models, and a description of the experimental methods used. The chapter after that discusses numerical, analytical and experimental results obtained. The last section is a conclusion of the study and lists possible areas for future work.

Chapters 3 and sections of chapters 4 and 5, have been submitted for IROS 2017 in a paper titled *"Magnetic Hammer Actuation for Tissue Penetration using Millirobot"*, which is currently under review. This paper focuses on the design of the millirobot and initial experiments. Another paper titled *"Validation of Control Methods for Magnetic Hammer Millirobot Actuation"* is under preparation and will cover the testing and validation of the three control strategies explained in Chapter 4.

Chapter 2

Literature Review

This chapter presents a review of existing literature that is relevant to the original work done as part of this thesis. The first section deals with different untethered micro- and millirobot designs for minimally invasive applications. The second section reviews current methods of modeling tissue penetration through needle insertion. Though these models provide valuable insights into the mechanics of tissue penetration, they cannot be directly adopted for the millirobot design discussed in this thesis. The reasons for this are explained in the second section as well. The third and final section deals with the optimal control of a vibratory piledriver to maximize its output force. The millirobot design presented in this paper uses a similar oscillating mechanism to produce pulsed forces for tissue penetration. Given the limited magnetic gradient strength available in the MRI, providing an optimal control input to the millirobot could produce much higher penetration forces.

2.1 Magnetic actuation of miniature, untethered robots

As mentioned in Chapter 1, many recent studies have been dedicated to the wireless control of miniature, untethered robots for MIS applications, using magnetic fields. The most commonly studied methods of propulsion have been torque generation using a rotational magnetic field, and force generation using magnetic field gradients. One of the first studies in the former field was by Honda et al. (1996), who proposed a microrobot design that consisted of a spiral Copper wire with a cubic permanent magnet at one end [9]. The mechanism rotates due to magnetic torque and the spiral design caused it to move linearly, much like a corkscrew. The linear velocity increased with the excitation frequency of the external rotating magnetic field. Further studies by Sendoh et al. (2002) extended this concept and demonstrated the individual directional control of micromachines [10]. In their designs, the linear motion was achieved using an external rotational magnetic field. In separate studies, Sendoh et al. (2002) and Sato et al. (2002) demonstrated the inclusion of heating elements in their micromachine designs, which could be used for local hyperthermia [11, 12]. These elements were heated using alternating magnetic fields. Explicit temperature sensing was compensated for by using heating elements with predefined Curie temperatures. Dreyfus et al. (2005) enabled the propulsion of a red blood cell in the presence of external uniform and rotating magnetic fields, by attaching a linear chain of molecules to the cell [13]. This was inspired by the propulsion mechanisms found in microorganisms such as bacteria and eukaryotic cells . These organisms use hair-like structures known as flagella, which are found in multiple structures and exhibit different movement patterns. Abbott et al. (2009) demonstrated that a helical propeller becomes preferable to pulling with magnetic field gradients as microrobot size decreases or as the distance from the magnetic field sources increases [14]. However, an external rotating magnetic field is required to propel a helical microrobot. The aim of our project however, is to enable millirobot control within an MRI scanner which has constant magnetic gradients in all three Cartesian directions. Simultaneous imaging is an added advantage which can be used as a real-time sensing modality. A rotational magnetic field would require additional hardware within the MRI environment, while using gradient based pulling would require only a software upgrade for the MRI scanner [15].

Early studies on magnetic gradient based pulling and tissue penetration were done by Grady et al. (1989) and Molloy et al. (1990) . They demonstrated the movement of a milli-scale devices of spherical and cylindrical shapes using a customized external magnetic gradient field, for local hyperthermia . The devices were used to penetrate canine brain tissue and phantom gelatin. However, the gradient field strength required to achieve penetration was 8 T/m. This is much more than what current MRI scanners can offer, which generate gradient fields in the range of 20 to 40 mT/m. More recent studies have shown that navigation of miniature devices through the blood stream is possible with the gradient fields in commercial MRI scanners [4, 7, 16, 17]. Becker et al. (2015) developed self-assembled Gauss guns that generated impulsive forces by converting magnetic potential energy into kinetic energy [8]. These could be used for tissue penetration and were demonstrated to achieve higher penetration forces than normal gradient-based pulling. The drawback of this mechanism is that it is hard to re-assemble the mechanism after a single release. This thesis presents a magnetic hammer millirobot design that is able to achieve tissue penetration through repeated impacts of a magnetized sphere on an impact plate, using the gradient fields in MRI scanners.

2.2 Estimation of tissue penetration forces

Many studies have been dedicated to modeling tissue penetration forces for surgical needle insertion. Simone et al. (2002) proposed modeling the penetration force during constant velocity needle insertion as the combination of three different forces: tissue stiffness, friction and cutting [18]. The capsule stiffness was modeled as a non-linear spring, friction by a modified Karnopp model and cutting was assumed to be constant for a given needle-tissue combination. Forces were measured by mounting a load cell on the robot arm holding the needle. The idea was to compare real-time force data to the models to control the puncture of interior structures during robot-assisted interventions. This model was tested on a bovine liver for different needle diameters and tip types by Okamura et al. (2004) [19]. Bevel tipped needles were prone to more bending and were easily affected by variations in tissue density. Larger diameter needles required higher penetration forces due to increased cutting and friction force components. Mahvash and Dupont (2010) used a non-linear viscoelastic model to predict the relationship between tissue deformation and rupture force at different velocities [20]. Their model predicted that tissue penetration forces could be reduced by increasing insertion velocities. This was proven experimentally as well. Other models have considered effects of needle insertion velocities, friction during the cutting phase and velocity-dependent cutting forces. While these models offer valuable insights into tissue penetration through quasi-static needle insertion, they cannot directly be adopted for our magnetic hammer millirobot due to its highly dynamic nature. This thesis does not cover the modeling of tissue penetration forces. However, this would prove valuable and we intend to perform tissue indentation tests in the future.

Chapter 3

Forces on the Millirobot

3.1 Mechanical model

The motion of the sphere between two consecutive impacts can be divided into two phases, based on the forces that act on it. The magnetic gradient force F_{mag} and friction force $F_{friction}$ act on the sphere during its motion along the free length of the tube, L (See Fig. 3.1 (i),(iii)). When the spring is compressed, its reaction force F_{spring} acts on the ball as well (See Fig. 3.1 (ii)). The directions of F_{mag} and $F_{friction}$ change depending on the direction of motion of the sphere.

Inside the homogeneous region of an MRI scanner, the magnitude of F_{mag} is constant [21]. The same has been assumed for developing analytical and numerical models in this paper. The formula for calculating F_{mag} is presented in section 3.2. Friction is considered to be negligible, but the assumption will be relaxed in later sections. The spring force is straightforward, and is given by

$$F_{spring} = kx, \tag{3.1}$$

where x is the compression length, and k is the spring constant.

3.2 Magnetic field calculation

The magnetic field generated by an MRI scanner can be separated into two components. The first is a constant and strong magnetic field B_0 along the z-axis. This field is used to align the magnetic moments of the protons. Commercial MRI scanners have B_0 typically ranging from 1.5 to 3 T. The second component of the

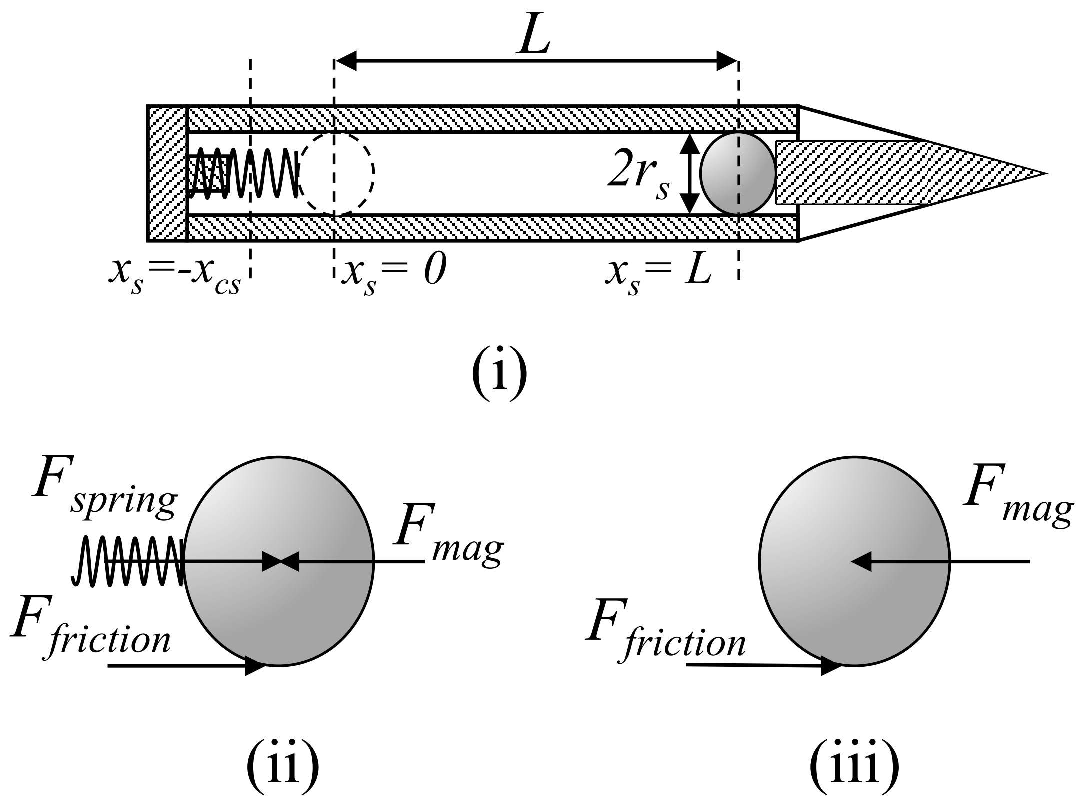

Figure 3.1: (i) Free length of sphere travel, L; (ii) Free body diagram of sphere when spring is compressed, (iii) when spring is not compressed

field is the magnetic gradient. It is used to encode the MRI signal spatially. The flux density $\mathbf{G}$ produced by the gradient coils is added to $\mathbf{B_0}$ and linearly varies with position. A computer controls this value. The total field inside the uniformity sphere of an MRI scanner is given by

$$\mathbf{B} = \mathbf{B_0} + \mathbf{G}. \tag{3.2}$$

$\mathbf{B_0}$ is given by

$$\mathbf{B_0} = \begin{bmatrix} 0 \\ 0 \\ B_0 \end{bmatrix}, \tag{3.3}$$

and $\mathbf{G}$, which is directly proportional to the current inside the gradient coils, is given by

$$\mathbf{G} = \begin{bmatrix} k_x I_x \\ k_y I_y \\ k_z I_z \end{bmatrix}. \tag{3.4}$$

In the above equation, k_x, k_y and k_z are the coil constants (T/A) and I_x, I_y and I_z are the electrical current values.

The flux density is more complicated to calculate outside of the uniformity sphere. The same problem is present in our desktop experiment because the flux density and gradient are not constant. To calculate forces accurately, it is necessary to compute the magnetic field precisely. A semi analytical method was used to calculate the field produced in all space by a solenoid assembly. It was tested on our desktop experiment.

According to [22], the magnetic flux density produced by a current loop in all space can be calculated using equations (3.5)-(3.8) and Fig. 3.2. $E(k)$ and $K(k)$ are the complete elliptical integrals of first and second kind respectively. B_z can be expressed as

$$B_z = \frac{\mu_0 I}{2\pi\delta^2\beta}\left[\left(a^2 - \rho^2 - z^2\right)\left(E(k^2) + \delta^2 K(k^2)\right)\right]. \tag{3.5}$$

B_θ can be expressed as

$$B_\theta = \frac{\mu_0 I \cdot z}{2\pi\delta^2\beta\rho}\left[\left(a^2 - \rho^2 - z^2\right)\left(E(k^2) - \delta^2 K(k^2)\right)\right]. \tag{3.6}$$

where δ is given by

$$\delta = \sqrt{a^2 + R_m^2 + Z_m^2 - 2aR_m}, \tag{3.7}$$

and β is given by

$$\beta = \sqrt{a^2 + R_m^2 + Z_m^2 + 2aR_m}. \tag{3.8}$$

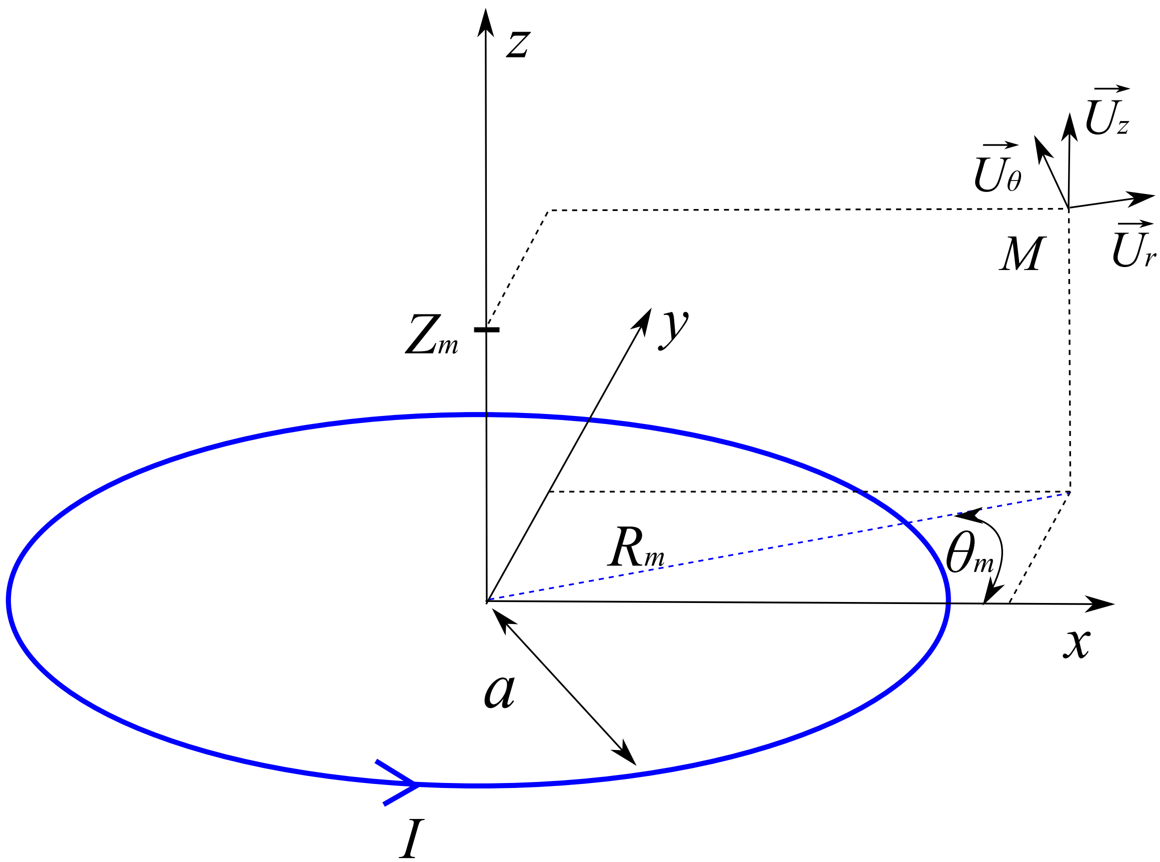

Figure 3.2: Geometry and variables used in equations (3.5)-(3.8)

The cross-section S of any solenoid can be divided into infinitesimal sections dS. Each dS is subjected to a current $dI = JdS$. This current dI forms an infinitesimal loop, and the field it produces can be calculated using (3.5)-(3.8). By integrating this equation over the solenoid cross-section, one can obtain the value of the flux density generated by the solenoid.

The flux density must be calculated for each solenoid. The total flux density is the vectorial sum of the flux density produced by each solenoid. The results obtained via this semi analytical method is compared to the solution obtained via finite element calculations with the software FEMM [23] (see fig. 3.3). The results are identical. The semi-analytical method is faster to compute for this model. Indeed, the magnetic field only needs to be calculated at the sphere position. The semi-analytical method can calculate the magnetic field at one point only whereas, finite elements methods

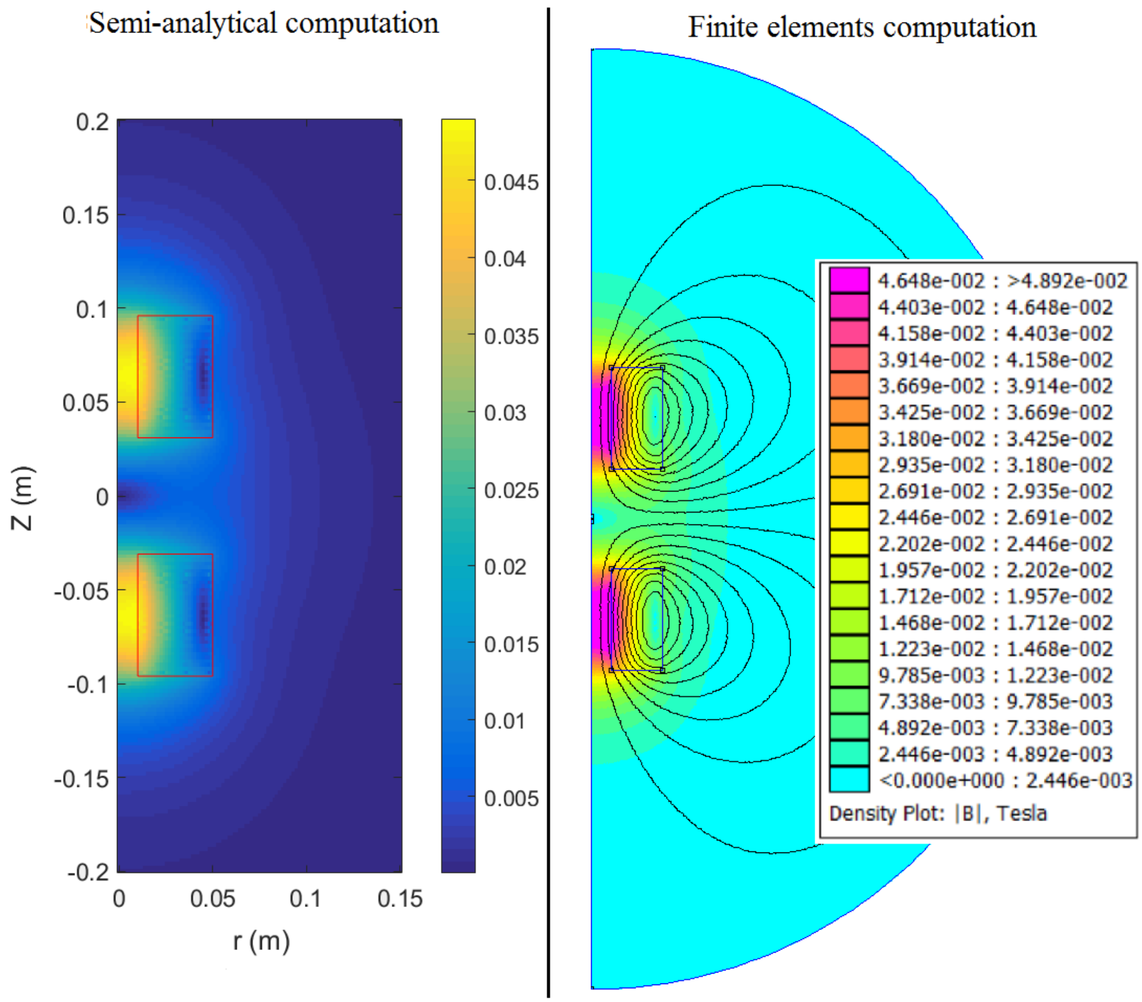

Figure 3.3: Comparison between the flux density computed with the semi-analytical method with MATLAB and the flux density computed via a finite element method with FEMM.

must compute the magnetic field in the full domain.

3.3 Magnetic force calculation

This section calculates the force applied by the magnetic field to the sphere.

The ferromagnetic sphere is small compared to the coil system and can be considered as a infinitely small magnetic moment $\mathbf{m}$. Assuming a constant material magnetization $\mathbf{M}$, one can calculate $\mathbf{m}$ from (3.9). V is the volume of the sphere. The ferromagnetic sphere is magnetized by the externally applied field $\mathbf{H}_{app} = \mathbf{B}_{app}/\mu_0$. Ferromagnetic materials create a demagnetizing field $\mathbf{H}_d$ when subjected to an external field. The actual field $\mathbf{H}$ seen by the sphere is the sum of $\mathbf{H}_{app}$ and $\mathbf{H}_d$. This effect must be taken into account to calculate the magnetization accurately. $\mathbf{H}_d$ is related to $\mathbf{H}_{app}$ by (3.10). The demagnetization factor N for a sphere is -1/3. Its magnetization can be calculated using (3.11). Once the magnetic moment $\mathbf{m}$ is obtained, the force on the sphere can be calculated using (3.12). $\mathbf{m}$ is given by

$$\mathbf{m} = \mathbf{M}.V \tag{3.9}$$

$\mathbf{H}_d$ is expressed as

$$\mathbf{H}_d = N.\mathbf{H}_{app}. \tag{3.10}$$

$\mathbf{M}$ is expressed as

$$\mathbf{M} = \frac{\mathbf{H}_{app}\,(\mu_r - 1)}{2.N.\mu_r - 1}, \tag{3.11}$$

and $\mathbf{F}$ is expressed as

$$\mathbf{F} = \nabla(\mathbf{m}.\mathbf{B}). \tag{3.12}$$

3.4 Buoyancy

The millirobot needs to be neutrally buoyant to float in the medium it travels through. To satisfy this condition, the weight of the magnetic hammer needs to be equal to the buoyant force. Assuming blood as the medium, the condition for neutral buoyancy is represented by (3.13) as

$$m_{mr} = \rho_b V_{mr}. \tag{3.13}$$

m_{mr}, ρ_b and V_{mr} represent the mass of the entire millirobot, density of blood and volume of blood displace by the millirobot, respectively.

Chapter 4

Control Strategies - Analytical and Numerical Results

4.1 Ideally closed-loop system

To maximize the average impact velocity over an arbitrary n number of contacts, the input magnetic gradient should always be in the same direction as the motion of the sphere. This is equivalent to a perfectly closed-loop system where the gradient signal switches direction when the sphere switches direction. An analytical model was developed by solving the system ODE to predict the impact velocity for each impact, given a set of input parameters. The sphere-impact plate system is assumed to have a coefficient of restitution, e. This model assumes that the robot capsule does not move. The impact velocities for different values of e are plotted in Fig. 4.1. For all values of e, the impact velocity initially increases and ultimately saturates, reaching a resonant value. This happens when the energy lost by the sphere during impact equals the energy gained by it during the rest of the cycle. As expected, a higher e results in a higher impact velocity. Fig. 4.2 shows a sample closed-loop pulsed magnetic gradient input for 50 impacts. The frequency initially varies until it settles to a constant value at resonance. An analytical formula was derived to predict the resonant impact velocity, for a given set of input parameters. This is expressed as

$$v_{res} = \frac{2\sqrt{\frac{F_{mag}\left((e^2+1)F_{mag}-kL(e^2-1)+\sqrt{(2-2e^4)kLF_{mag}+(1+e^2)^2F_{mag}^2}\right)}{km_s}}}{1-e^2}. \tag{4.1}$$

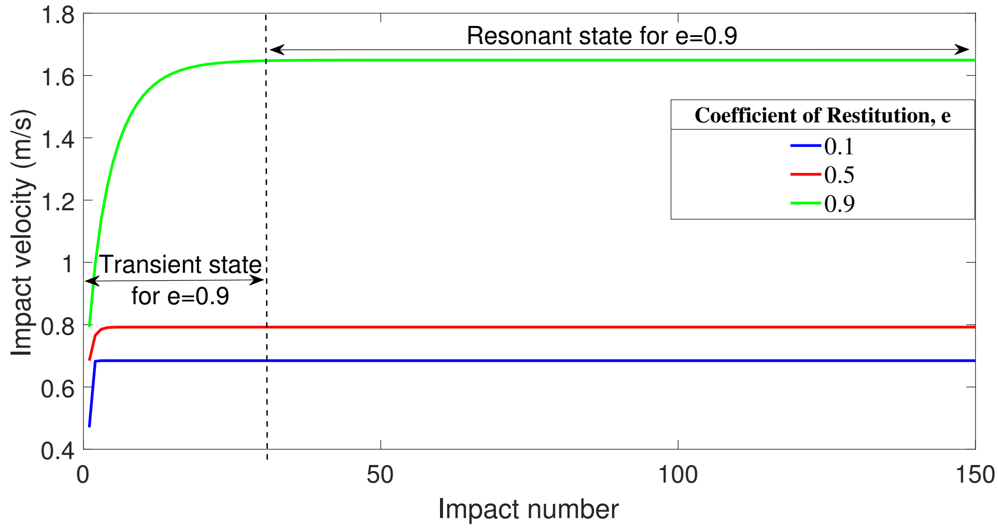

Figure 4.1: Closed loop impact velocity for 150 impacts; k = 50 N/m; e = 0.9; F_{mag} = 1.5e-3 N; L = 0.03 m; m_s = 5.58e-4 kg; r_s = 2.5 mm.

In the above equation, m_s is the mass of the sphere in kilograms. The radius of the ball r_s indirectly influences the impact velocity through F_{mag} and m_s, both of which depend on the volume of the sphere. The variation of v_{res} with changes in $L, e, k, m_s, r_s, F_{mag}$ were plotted and they were all found to be monotonic functions with no critical points. From eqn. (4.1), it is seen that $v_{res} \to \infty$ as $e \to 1$. This is expected because $e = 1$ represents a perfectly elastic collision with no energy lost during the collision. Hence, the impact velocity increases with every impact. Further, the time between impacts at resonance t_{res}, is a constant value and is expressed as

$$t_{res} = t_{pos,1} + t_{pos,2} + t_{ant,1} + t_{ant,2}, \tag{4.2}$$

where $t_{pos,1}$, $t_{pos,2}$, $t_{ant,1}$, $t_{ant,2}$, x_{cs} and ω are expressed as follows:

$$t_{pos,1} = \frac{\sqrt{e^2 v_{\text{res}}^2 + \frac{2LF_{\text{mag}}}{m_s}} - ev_{\text{res}}}{\frac{F_{\text{mag}}}{m_s}}, \tag{4.3}$$

$$t_{pos,2} = \frac{\pi - \tan^{-1}\left(\frac{k\sqrt{e^2 v_{\text{res}}^2 + \frac{2LF_{\text{mag}}}{m_s}}}{\omega F_{\text{mag}}}\right)}{\omega}, \tag{4.4}$$

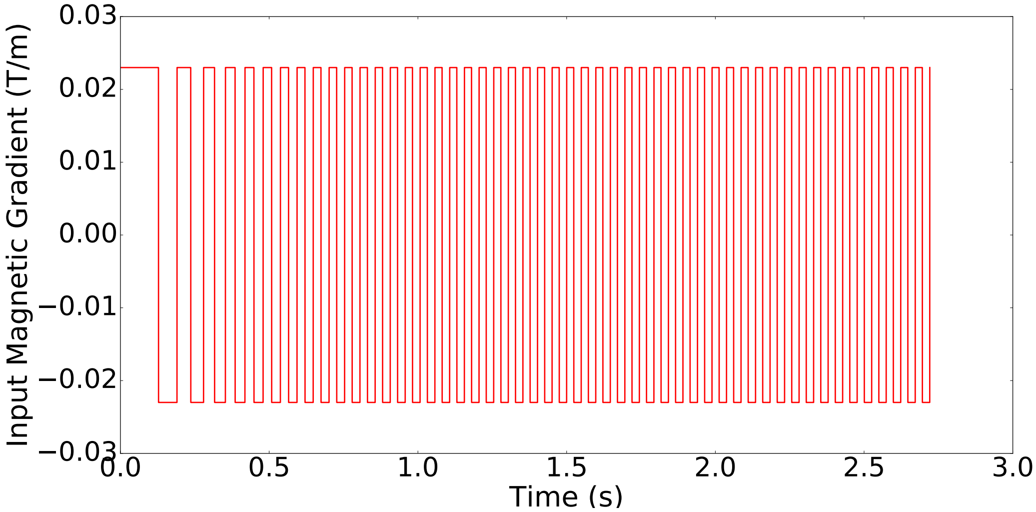

Figure 4.2: Closed loop input gradient for 50 impacts; k = 50 N/m; e = 0.9; F_{mag} = 1.5e-3 N; L = 0.03 m; m_s = 5.58e-4 kg; r_s = 0.0025 m.

$$t_{ant,1} = \frac{\cos^{-1}\left(\frac{F_{\text{mag}}}{F_{\text{mag}}+kx_{cs}}\right)}{\omega}, \tag{4.5}$$

$$t_{ant,2} = \frac{v_{\text{res}} - \sqrt{v_{\text{res}}^2 - \frac{2LF_{\text{mag}}}{m_s}}}{\frac{F_{\text{mag}}}{m_s}}, \tag{4.6}$$

$$x_{cs} = \frac{\sqrt{e^2 k m_s v_{\text{res}}^2 + 2kLF_{\text{mag}} + F_{\text{mag}}^2} + F_{\text{mag}}}{k}, \text{ and} \tag{4.7}$$

$$\omega = \sqrt{\frac{k}{m_s}}. \tag{4.8}$$

In the above equations, x_{cs} is the maximum compression distance of the spring (See Fig. 3.1 (i)), and ω represents the natural frequency of the spring-mass system. The value of x_{cs} can be used to select an appropriate free length for the spring, to ensure that it does not bottom out during compression. The values $t_{pos,1}$, $t_{pos,2}$, $t_{ant,1}$ and $t_{ant,2}$ represent the time for the ball to move from x_S = (i) L to 0, (ii) 0 to $-x_{cs}$, (iii) $-x_{cs}$ to 0, and (iv) 0 to L respectively, in a perfectly closed-loop system with optimal gradient switching. To effectively compare the results between different control strategies, the following parameter values have been assumed: k = 50 N/m,

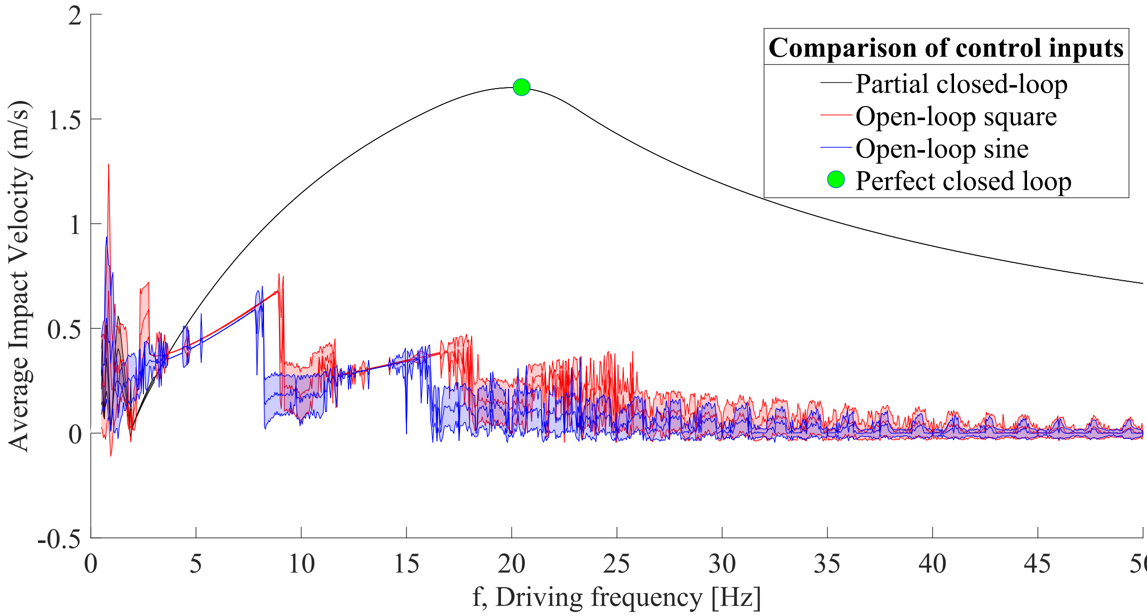

Figure 4.3: Comparison of average impact velocities between impacts 100 and 1100 for three different control inputs: Open-loop vs. Partially closed-loop vs. Ideally closed-loop

$e = 0.9$, $F_{mag} = 1.5\text{e-}3$ N, $L = 0.03$ m, $m_s = 5.58\text{e-}4$ kg, $r_s = 2.5$ mm. For these parameters, the average impact velocity for an ideally closed-loop system over 1000 impacts, has been plotted as the green circle in Fig. 4.3.

4.2 Partially closed-loop system

4.2.1 Zero friction model

With sensing at both ends, we can implement an ideally closed-loop system where the magnetic gradient force is always in the same direction as the motion of the ball. However, practically realizing perfect sensing at both the posterior and anterior ends of the capsule is difficult. This motivated us to simulate a partially closed-loop system which only senses impacts at the anterior end, while leaving the switching time at the posterior end t_s, to manual control. Experimentally, this was realized by using a laser diode-receiver pair at the anterior end which detected the sphere

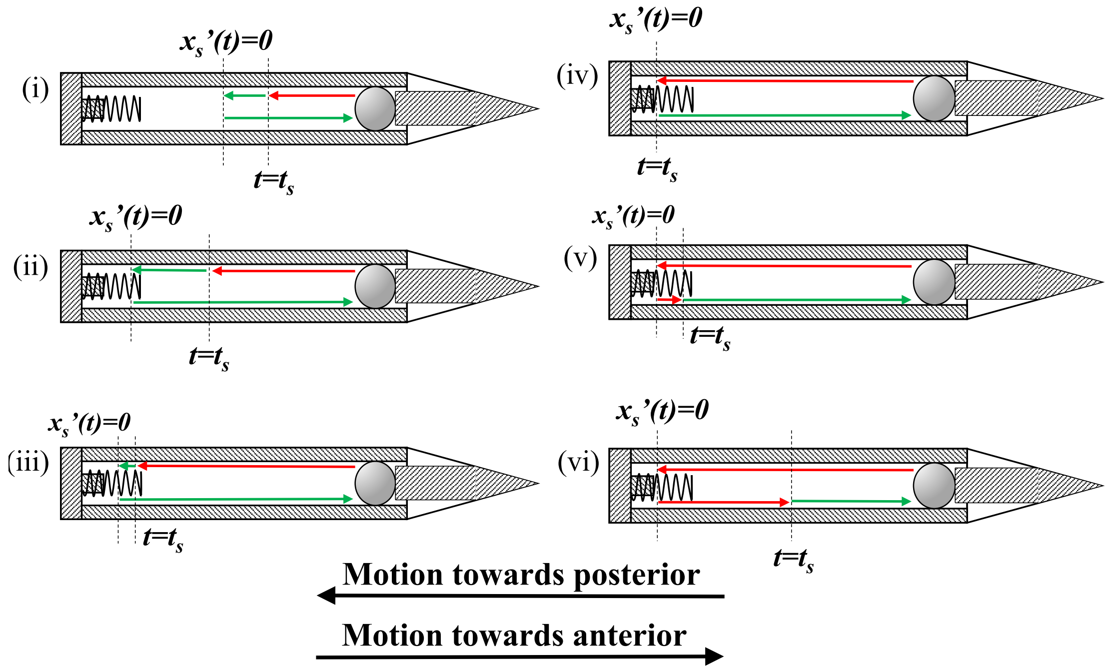

Figure 4.4: Six domains for spring-end switching time; green and red represent F_{mag} towards anterior and posterior respectively. Direction of colored arrow represents direction of ball motion.

impacts. The switching time at the posterior end t_s, was varied and the resultant average impact velocities are plotted in fig. 4.3. In this figure, the x-axis represents the driving frequency f, where $f = 1/(2t_s)$. The average impact velocity increases and reaches a maximum when the partial closed-loop switching frequency is equal to the ideal closed-loop switching frequency. This shows that a partially closed-loop system tuned to the right frequency can produce the same average impact velocity as an ideal-closed loop system, assuming all other system parameters are the same. However, this model works only for cases where the Coulomb friction force is low. An analytical model was developed to express the time between two successive impacts Δt, as a function of the posterior switching time t_s, initial (post-impact) velocity v_{o^+}, and other parameters such as L, k, a and m_s, where a is the acceleration on the sphere due to F_{mag}. The expression is of the form

$$\Delta t(t_s, v_{o^+}, a, m_s, k, L) = \begin{cases} \Delta t_1(t_s, v_{o^+}, a, L), & v_{o^+}^2 < 2aL \quad \& \quad t_s < t_{\mathrm{c1}} \\ \Delta t_2(t_s, v_{o^+}, a, m_s, k, L), & t_{\mathrm{c1}} \le t_s \le t_{\mathrm{c2}} \\ \Delta t_3(t_s, v_{o^+}, a, m_s, k, L), & t_{\mathrm{c2}} < t_s < t_{\mathrm{c3}} \\ \Delta t_4(t_s, v_{o^+}, a, m_s, k, L), & t_s = t_{\mathrm{c3}} \\ \Delta t_5(t_s, v_{o^+}, a, m_s, k, L), & t_{\mathrm{c3}} < t_s < t_{\mathrm{c4}} \\ \Delta t_6(t_s, v_{o^+}, a, m_s, k, L), & t_{\mathrm{c4}} \le t_s < t_{\mathrm{c5}} \\ t_{\mathrm{c5}}, & t_{\mathrm{c5}} \le t_s \end{cases} . \quad (4.9)$$

In eqn. (4.9), Δt_n for $n = 1$ to 6 represent six possible and relevant cases of ball motion based on the value of t_s. These six cases are illustrated in Fig. 4.4. In Fig. 4.4(i), the initial velocity v_{0^+} and t_s are low enough that the sphere reverses direction before reaching the spring. In this case, $v_{0^+} < 2aL$, where $a = F_{mag}/m_s$. Fig. 4.4(ii) represents the case when v_{0^+} is high enough that spring compression is unavoidable even for $t_s = 0$. In Fig. 4.4(iii), the signal switch happens after spring compression starts but before it bottoms out. Fig. 4.4(iv) represents perfect closed loop switching. In Fig. 4.4(v), the signal is switched after maximum compression, but before the sphere reaches $x_s = 0$. Fig. 4.4(vi) represents switching after spring rebound and before the next impact. There is also a possible seventh case where the switching happens after one entire impact cycle. This case is not relevant and serves more as an upper limit of practical t_s values. t_{cn} values for $n = 1$ to 5 are the threshold switching time values for each case. These are calculated by analytically solving the first order ODE for each case. The seven cases of motion are divided by five different threshold values for t_s which are expressed as follows:

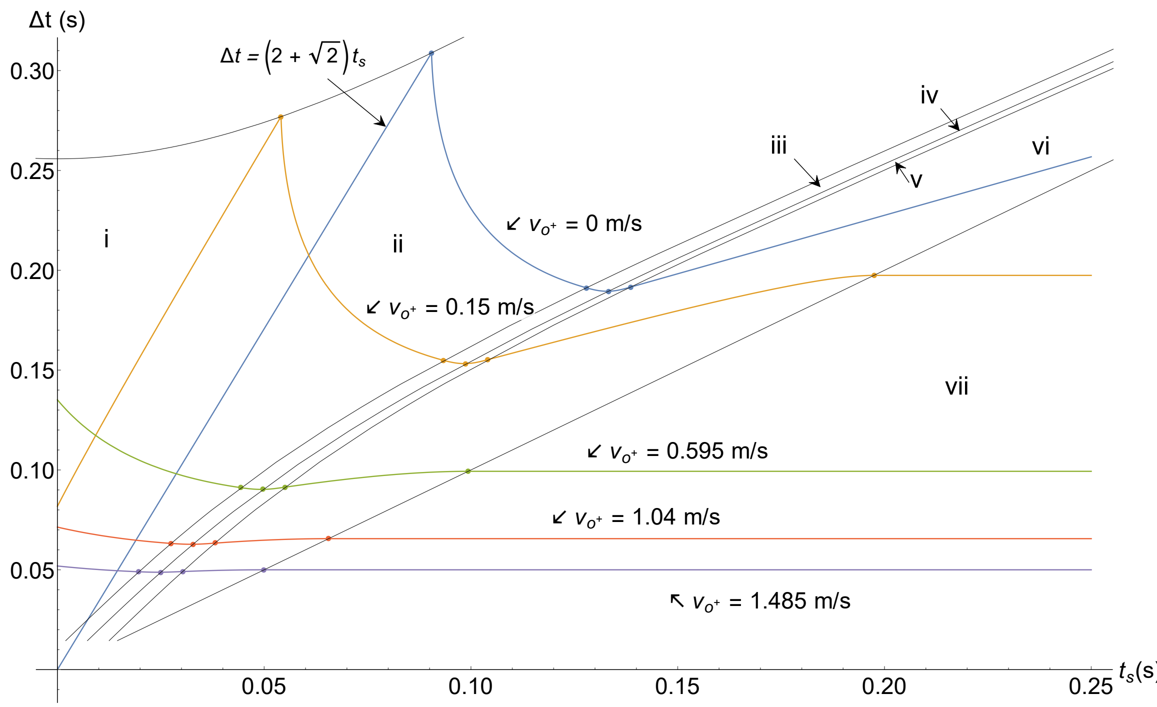

Figure 4.5: Plot of Δt vs. t_s for different values of v_{o^+}.

$$t_{c1} = \frac{\sqrt{4aL + 2v_{o^+}^2} - 2v_{o^+}}{2a}, \tag{4.10}$$

$$t_{c2} = \frac{\sqrt{2aL + v_{o^+}^2} - v_{o^+}}{a}, \tag{4.11}$$

$$t_{c3} = \frac{\pi - \tan^{-1}\left(\frac{k\sqrt{2aL+v_{o^+}^2}}{a\sqrt{km_s}}\right)}{\sqrt{\frac{k}{m_s}}} + t_{c2}, \tag{4.12}$$

$$t_{c4} = \frac{2\left(\pi - \tan^{-1}\left(\frac{k\sqrt{2aL+v_{o^+}^2}}{a\sqrt{km_s}}\right)\right)}{\sqrt{\frac{k}{m_s}}} + t_{c2}, \text{ and} \tag{4.13}$$

$$t_{c5} = 2t_{c3}. \tag{4.14}$$

The variation of Δt with t_s for different values of v_{o^+} are plotted in Fig. 4.5. For this plot, the same parameter values as in section 4.1 have been assumed. The regions labeled (i) to (vii) represent the respectively numbered cases in eqn. 4.9. Region (i) is bounded by the black line on top, and the line $\Delta t = (2 + \sqrt{2})t_s$ on the right side. Case (iv) represents the ideal closed-loop switching time and is illustrated by the middle line among the three almost-parallel lines.

Analytical expressions for equation (4.9)

For all six cases of Δt, F_{mag} and ω are constant. ω represents the natural frequency of the spring-mass system and is expressed as

$$\omega = \sqrt{\frac{k}{m_s}}. \tag{4.15}$$

F_{mag} is the force applied by the external magnetic system and is expressed as

$$F_{\mathrm{mag}} = m_s a. \tag{4.16}$$

In the following expressions, $v_{i,j}$ represents the sphere velocity in m/s at a certain point during the impact cycle. Here, i represents the case number and takes values from 1 to 6. j represents different phases within each case and is chosen for convenience. Similarly, $s_{i,j}$ represents displacement in meters, and $t_{i,j}$ the duration of motion in seconds. $y_{i,0}$ represents the maximum length of spring compression in meters for each case. All other parameters have been previously defined.

Expression for Δt_1:

Δt_1 is expressed as

$$\Delta t_1 \left(t_s, v_{o^+}, a, L\right) = \sqrt{2\left(\left(\frac{v_{o^+}}{a} + t_s\right)^2 - \frac{v_{o^+}^2}{2a^2}\right)} + \frac{v_{o^+}}{a} + 2t_s. \tag{4.17}$$

Expression for Δt_2:

Δt_2 is expressed as

$$\Delta t_2 \left(t_s, v_{o^+}, a, m_s, k, L\right) = t_{2,1a} + t_{2,2a} + t_{2,1b} + t_{2,2b} + t_s, \tag{4.18}$$

where $t_{2,1a}$, $t_{2,2a}$, $t_{2,1b}$ and $t_{2,2b}$ are given by the following equations:

$$t_{2,1a} = \frac{v_{2,\mathrm{ts}} - v_{2,1a}}{a}, t_{2,2a} + t_{2,1b} = \frac{2}{\omega} \tan^{-1}\left(\frac{k v_{2,1a}}{\omega F_{\mathrm{mag}}}\right), \textit{ and} \tag{4.19}$$

$$t_{2,2b} = \frac{\sqrt{v_{2,1a}^2 + 2aL} - v_{2,1a}}{a}. \tag{4.20}$$

$v_{2,1a}$ and $s_{2,1}$ in the above equations are given by the following equations:

$$v_{2,1a} = \sqrt{v_{1,\mathrm{ts}}^2 - 2a\left(L - s_{2,1}\right)}, \textit{ and} \tag{4.21}$$

$$s_{2,1} = \frac{a t_s^2}{2} + v_{o^+} t_s. \tag{4.22}$$

Expression for Δt_3:

Δt_3 is expressed as

$$\Delta t_3\left(t_s, v_{o^+}, a, m_s, k, L\right) = t_{3,2a} + t_{3,2b} + t_s, \tag{4.23}$$

where the terms on the right hand side are given by the following equations:

$$\tag{4.24}$$

$$t_{3,2a} = \frac{2}{\omega} \tan^{-1}\left(\frac{\sqrt{k\left(2\omega^2 F_{\mathrm{mag}} y_{3,\mathrm{t1b}} + k v_{3,\mathrm{t1b}}^2 + k\omega^2 y_{3,\mathrm{t1b}}^2\right)} + k v_{3,\mathrm{t1b}}}{\omega\left(k y_{3,\mathrm{t1b}} + 2F_{\mathrm{mag}}\right)}\right), \textit{ and} \tag{4.25}$$

$$t_{3,2b} = \frac{\sqrt{v_{3,2a}^2 + 2aL} - v_{3,2a}}{a}. \tag{4.26}$$

The right hand side terms in the above two equations are given by the following equations:

$$\tag{4.27}$$

$$v_{3,\mathrm{t1b}} = \sqrt{2aL + v_{o+}^2}\cos\left(\omega t_{3,1b}\right) + \frac{\omega F_{\mathrm{mag}} \sin\left(\omega t_{3,1b}\right)}{k}, \tag{4.28}$$

$$y_{3,\mathrm{t1b}} = \frac{\sqrt{2aL + v_{o+}^2}\sin\left(\omega t_{3,1b}\right)}{\omega} - \frac{F_{\mathrm{mag}}\cos\left(\omega t_{3,1b}\right)}{k} + \frac{F_{\mathrm{mag}}}{k}, \tag{4.29}$$

$$v_{3,2a} = \sqrt{\frac{2y_{3,0}F_{\text{mag}}}{m_s} + \frac{ky_{3,0}^2}{m_s}}, \tag{4.30}$$

$$y_{3,0} = \frac{\sqrt{F_{\text{mag}}^2 - 2ck} - F_{\text{mag}}}{k}, \tag{4.31}$$

$$c = -2F_{\text{mag}}y_{3,\text{t1b}} - \frac{1}{2}m_s\left(2aL + v_{o^+}^2\right), \ \ \textit{and} \tag{4.32}$$

$$t_{3,1b} = t_s - t_{\text{c2}}. \tag{4.33}$$

c is a parameter assigned for conveniently presenting the calculations and has no specific significance with respect to the dynamics of the system.

Expression for Δt_4:

Δt_4 is expressed as

$$\Delta t_4\left(t_s, v_{o^+}, a, m_s, k, L\right) = t_{4,\text{for1}} + t_{4,\text{for2}} + t_s, \tag{4.34}$$

where the terms on the right hand side are given by the following equations:

$$t_{4,\text{for1}} = \frac{\cos^{-1}\left(\frac{F_{\text{mag}}}{ky_{4,0}+F_{\text{mag}}}\right)}{\omega}, \textit{and} \tag{4.35}$$

$$t_{4,\text{for2}} = \frac{v_{4,\text{imp}} - v_{4,4}}{a}. \tag{4.36}$$

The right hand terms in the above two equations are given by the following equations:

$$y_{4,0} = \frac{\sqrt{2kLF_{\text{mag}} + F_{\text{mag}}^2 + km_sv_{o^+}^2} + F_{\text{mag}}}{k}, \tag{4.37}$$

$$v_{4,\text{imp}} = \sqrt{v_{4,4}^2 + 2aL}, \ \ \textit{and} \tag{4.38}$$

$$v_{4,4} = \sqrt{\frac{2y_{4,0}F_{\text{mag}}}{m_s} + \frac{ky_{4,0}^2}{m_s}}. \tag{4.39}$$

Expression for Δt_5:

Δt_5 is expressed as

$$\Delta \mathrm{t}_5\left(t_s, v_{o^+}, a, m_s, k, L\right) = t_{5,2b} + t_{5,2c} + t_s. \tag{4.40}$$

where $t_{5,2b}$ and $t_{5,2c}$ are given by the following equations:

$$t_{5,2b} = \frac{2}{\omega}\tan^{-1}\left(\frac{\sqrt{k\left(2\omega^2 F_{\mathrm{mag}} y_{5,2a} + k v_{5,2a}^2 + k\omega^2 y_{5,2a}^2\right)} + k v_{5,2a}}{\omega\left(k y_{5,2a} + 2F_{\mathrm{mag}}\right)}\right), \;\; and \tag{4.41}$$

$$t_{5,2c} = \frac{v_{5,\mathrm{imp}} - v_{5,2b}}{a}. \tag{4.42}$$

The right hand side terms in the above two equations are given by the following equations:

$$v_{5,2a} = \frac{\omega F_{\mathrm{mag}} \sin\left(\omega t_{5,2a}\right)}{k} + \sqrt{2aL + v_{o^+}^2}\cos\left(\omega t_{5,2a}\right), \tag{4.43}$$

$$y_{5,2a} = -\frac{F_{\mathrm{mag}}\cos\left(\omega t_{5,2a}\right)}{k} + \frac{\sqrt{2aL + v_{o^+}^2}\sin\left(\omega t_{5,2a}\right)}{\omega} + \frac{F_{\mathrm{mag}}}{k}, \tag{4.44}$$

$$t_{5,2a} = t_s - t_{\mathrm{c}2}, \tag{4.45}$$

$$v_{5,\mathrm{imp}} = \sqrt{v_{5,2b}^2 + 2aL}, \;\; and \tag{4.46}$$

$$v_{5,2b} = \left\| v_{5,2a}\cos\left(\omega t_{5,2b}\right) - \left(\frac{F_{\mathrm{mag}}}{k} + y_{5,2a}\right)\omega\sin\left(\omega t_{5,2b}\right)\right\|. \tag{4.47}$$

Expression for Δt_6:

Δt_6 is expressed as

$$\Delta \mathrm{t}_6\left(t_s, v_{o^+}, a, m_s, k, L\right) = t_{6,2b} + t_s. \tag{4.48}$$

where $t_{6,2b}$ is expressed as

$$t_{6,2b} = \frac{v_{6,\mathrm{imp}} - v_{6,\mathrm{ts}}}{a}. \tag{4.49}$$

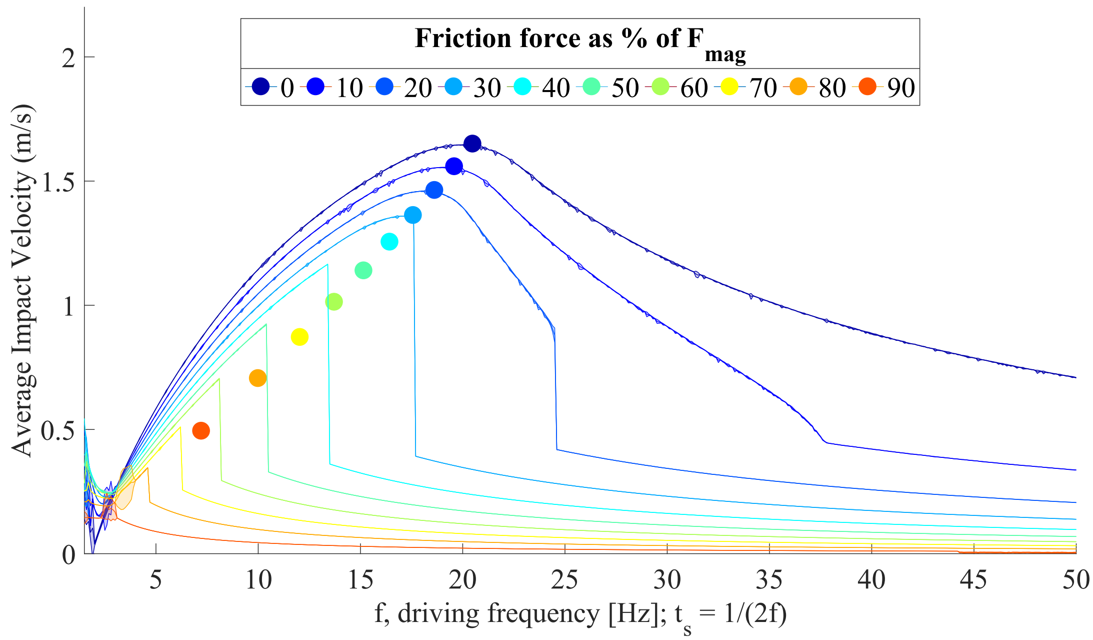

Figure 4.6: Comparison of simulated impact velocities. The velocities for impacts 100 to 200 are averaged and plotted for different values of Coulomb friction force. Colored circles represent the ideal closed-loop values. Lines represent the partially closed-loop values.

The right hand terms in the above equation are given by the following equations:

$$v_{6,\text{imp}} = \sqrt{2a\left(L - s_{6,\text{ts}}\right) + v_{6,\text{ts}}^2}, \tag{4.50}$$

$$s_{6,\text{ts}} = v_{6,1}\left(t_s - t_{6,1}\right) - \frac{1}{2}a\left(t_s - t_{6,1}\right)^2, \tag{4.51}$$

$$v_{6,\text{ts}} = v_{6,1} - a\left(t_s - t_{6,1}\right), \tag{4.52}$$

$$v_{6,1} = \sqrt{2aL + v_{o+}^2}, \text{ and} \tag{4.53}$$

$$t_{6,1} = t_{c4}. \tag{4.54}$$

4.2.2 Effect of Coulomb friction

In all the above models, the friction force was assumed to be zero. Average impact velocities over 100 impacts are plotted for varying values of the friction force in Fig. 4.6. The circles represent the ideally-closed loop values, while the curves represent the partially closed-loop values using impact times. Much like the step-

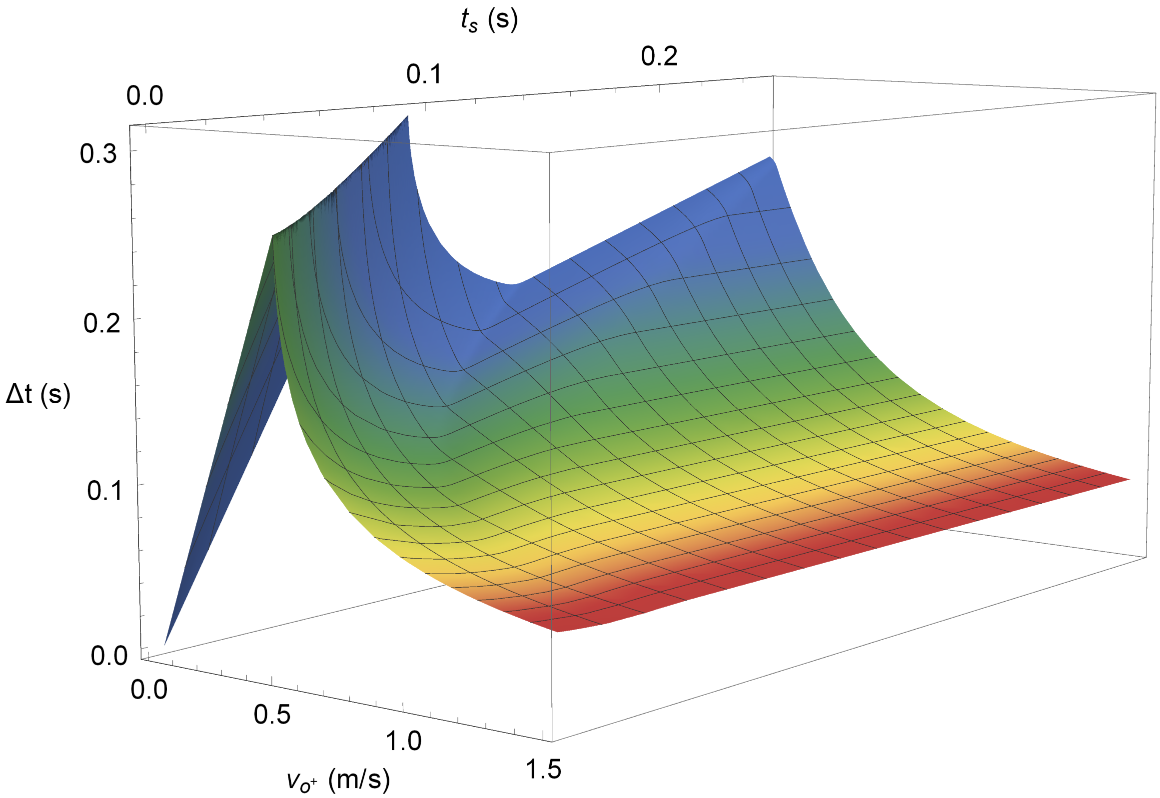

Figure 4.7: 3D contour plot of Δt vs. t_s plotted for different values of v_{o+}. t_s is a control parameter and Δt can be obtained by sensing. Together, Δt and t_s can be used to estimate v_{o+} with our estimator.

out frequency of a stepper motor, average impact velocities drop suddenly for the partially closed-loop system beyond a cut-off driving frequency. This is due to the sphere reversing direction before spring contact, leading to a drop in its net kinetic energy. As friction force increases as a percentage of F_{mag}, the partially closed loop system reaches its cutoff frequency, before resonance. This drop in impact velocity is not seen in the fully closed-loop system, for any values of friction. Hence, partially closed-loop control will not produce the maximum possible impact velocity for high values of Coulomb friction force.

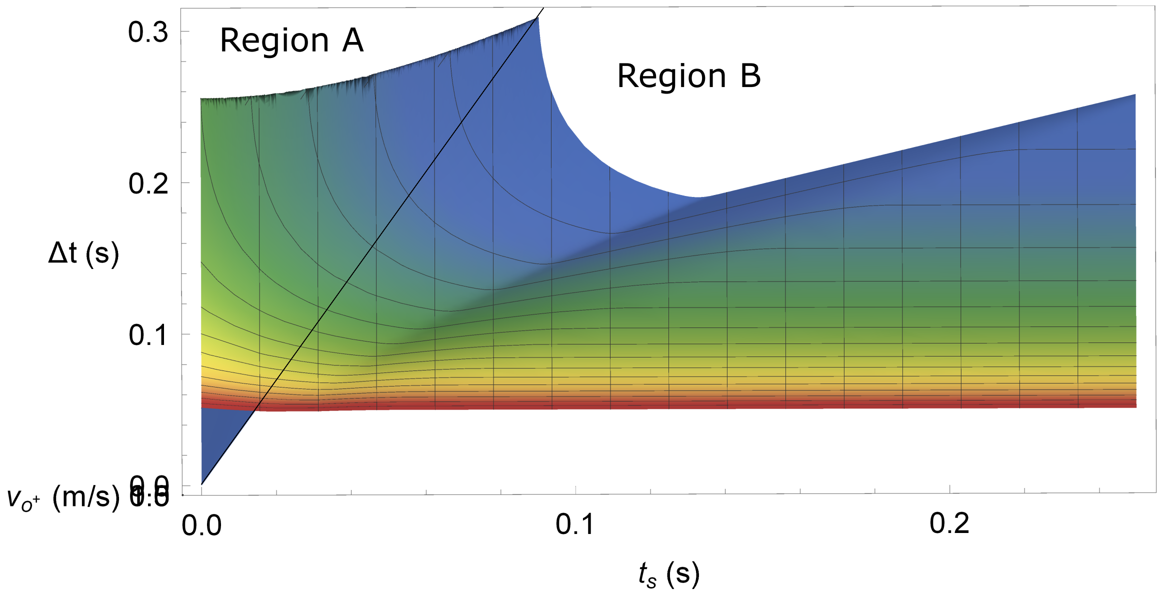

Figure 4.8: Side view of 3D contour plot in Fig. 4.7. If Δt and t_s are known, we can calculate v_{o+} in region B, or have two possible values in region A.

4.2.3 Post-impact velocity estimator

A 3D contour plot showing the variation of Δt with t_s for v_{o^+} values from 0 to 1.5 m/s, are shown in figures 4.7 and 4.8. There exists a unique v_{o^+}, or post-impact velocity, for low values of Δt and high values of t_s. In this case, the post-impact velocity can be easily estimated based on the measured Δt and t_s. However, for high values of Δt and low values of t_s, there exist two possible values of v_{o^+}. This is also seen in Fig. 4.5 at the points of intersection of the different v_{o^+} curves. Where there are two solutions, we can determine the post-impact velocity if we could detect contact of the sphere with the spring. The linear region represents the case where the ball reverses direction before spring compression. If the spring was compressed, we select the higher value for v_{o^+}. If not, we select the lower value for v_{o^+}, as seen in Fig. 4.5. The estimated values of post-impact velocity could be used to progressively tune t_s towards the ideal closed-loop value.

4.3 Open-loop control

In open-loop control, sinusoidal and square waveforms of constant frequencies are used for F_{mag}. The average impact velocity of the sphere over 1000 impacts is then calculated for a range of input frequencies as shown in Fig. 4.3. Excluding the transient region for frequencies between 0 and 2.5 Hz, the average impact velocity reaches a maximum between 5 and 10 Hz, for both the square and sinusoidal inputs. The lack of a continuous trend is expected because the duration of ball motion in both directions does not remain constant over 1000 impacts, as the open-loop frequency increases. For both inputs, there are short linear regions followed by sudden drops in the average impact velocity. Following the second drop, the average impact velocity seems to oscillate about a low value of about 0.2 m/s. As seen in Fig. 4.3, the maximum open-loop average impact velocity is about 3 times lower than the corresponding ideal closed-loop value. This validates the need for an ideally closed-loop system or tuning a partially closed-loop system.

Chapter 5

Experimental Setup and Results

5.1 Magnetic test bench description

A desktop-size, single-axis magnetic setup was built to reduce the cost related to clinical MRI experiments. It is composed of two solenoid coils oriented along the same axis and separated by a distance d. The coils are used to produce both the magnetizing field and the gradient. The properties of the coils are shown in Table 5.1.

The system is shown in Fig. 5.1. The two coils are held by an acrylic tube. They can slide along this tube and be locked in place to adjust the distance between the two coils and therefore change the maximum field and gradient values. The acrylic tube is transparent, allowing for visual access to the robot. Each coil is powered via a Syren 25 switch mode power supply. A Hall-effect-based current sensor is used to perform a PID regulation of the current. It is necessary to control the current inside the coils and not only the voltage. Indeed, the produced magnetic field is directly proportional to the current whereas the voltage is related to the magnetic flux variation and the voltage drop produced by Joule effect losses.

Robots are inserted inside the acrylic tube holding the coils. They are held by a second, smaller tube that guides them along the system axis. Robots can be free to move along the coil axis or held in place. A picture of the system is provided in Fig. 5.1.

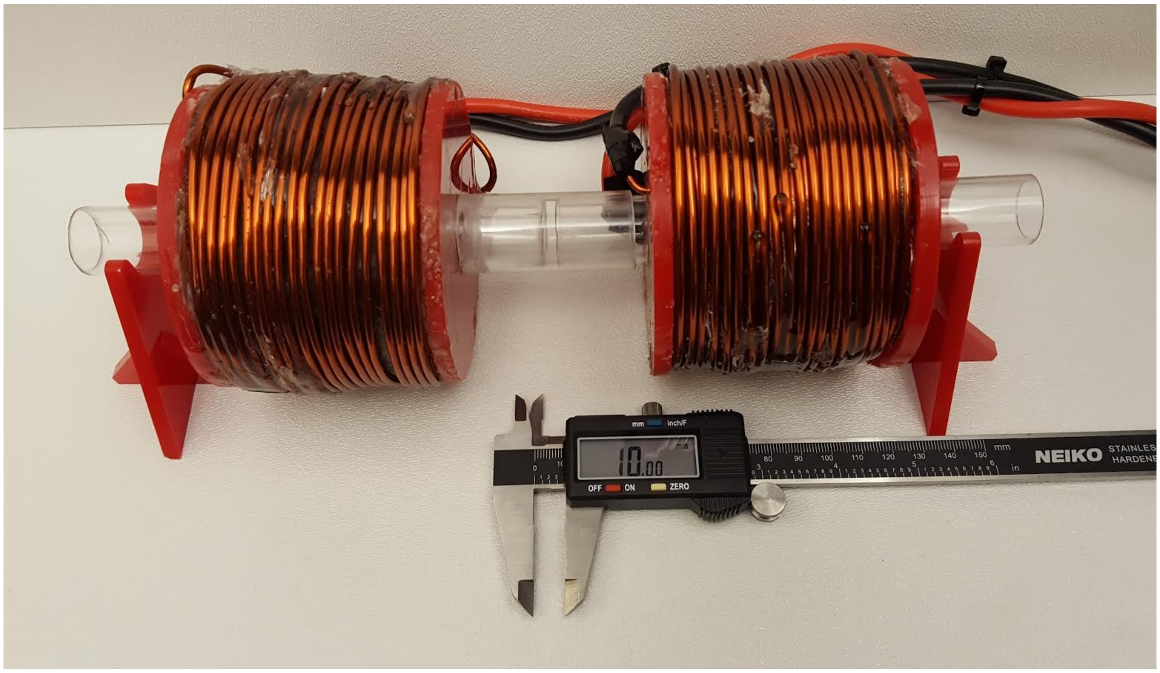

Figure 5.1: Picture of the desktop-size magnetic setup.

Table 5.1: Properties of the coils used in the desktop-size test bench

Internal Radius	12.7 mm	Electrical resistance	0.16 Ω
External Radius	45.8 mm	Inductance	1.59 mH
Length	65 mm	Max current change rate Voltage = 25 V	15.7 kA/s
Wire	10 AWG	Max continuous current	15 A
Wire cross-section	5.26 mm^2	Flux density on system center I = 15 A, d = 50 mm	11 mT
Number of turns	265	Gradient on system center I = 15 A, d = 50 mm	0.45 T/m

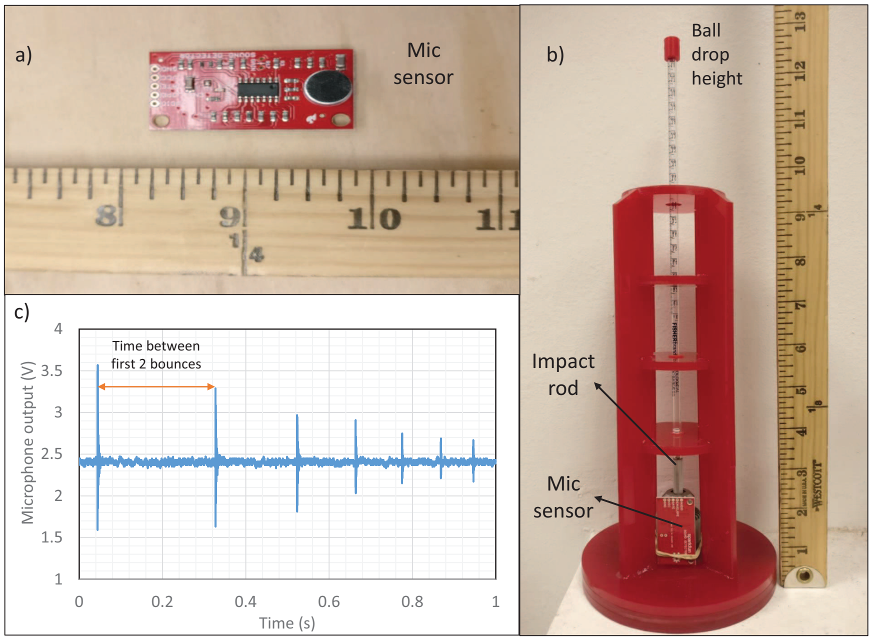

Figure 5.2: Experimental setup for measuring the coefficient of restitution e

5.2 Coefficient of restitution measurements

The coefficient of restitution e was determined using the time interval between two consecutive bounces of the sphere when dropped from a given height onto the impact rod. A microphone sensor was used to detect the impact. The measurements were made using short impact rods for five different materials. Three rod diameters were tested for all the materials: $\frac{1}{8}$", $\frac{3}{16}$" and $\frac{1}{4}$". Impact rods were held by a drill chuck. 15.0 mm of the impact rods were sticking out of the chuck. The experimental setup is shown in Fig. 5.2.

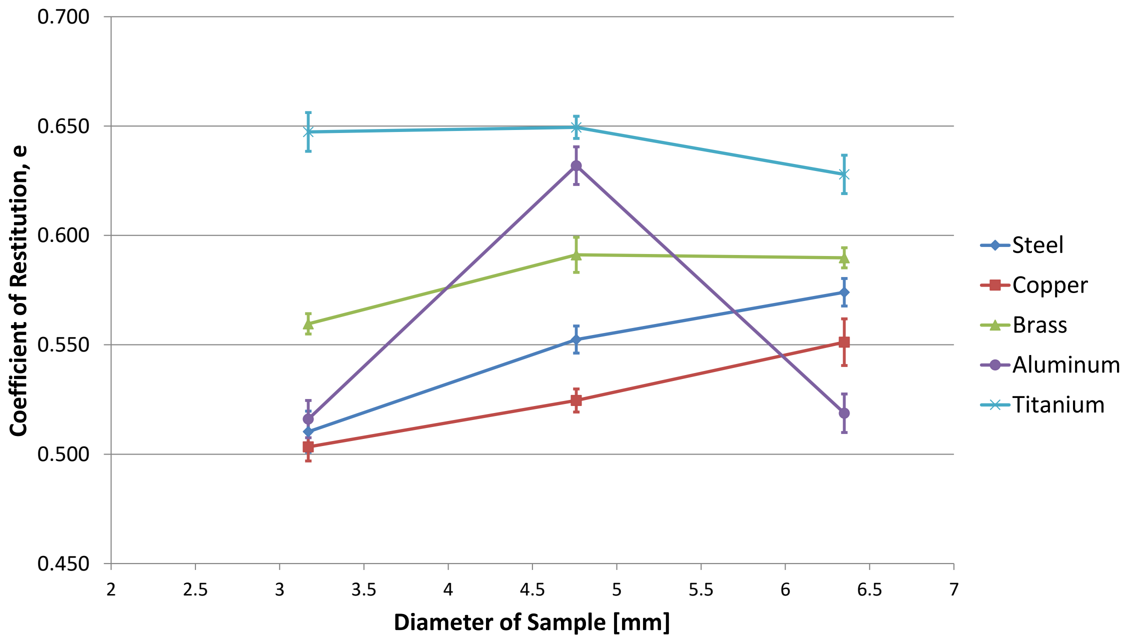

Figure 5.3: Measured coefficient of restitution e as a function of rod diameter for different materials

The results, shown in fig. 5.3, show that titanium offers the largest coefficient of restitution, for all three selected diameters. The densities of aluminum, titanium, stainless steel, brass, and copper are 2720, 4500, 7600, 8500, and 8940 kg/m^3 respectively. This data, coupled with a desire for a lightweight millirobot suggests that titanium is the best material for an impact plate. Bio-compatibility of the material used is another constraint that needs to be considered.

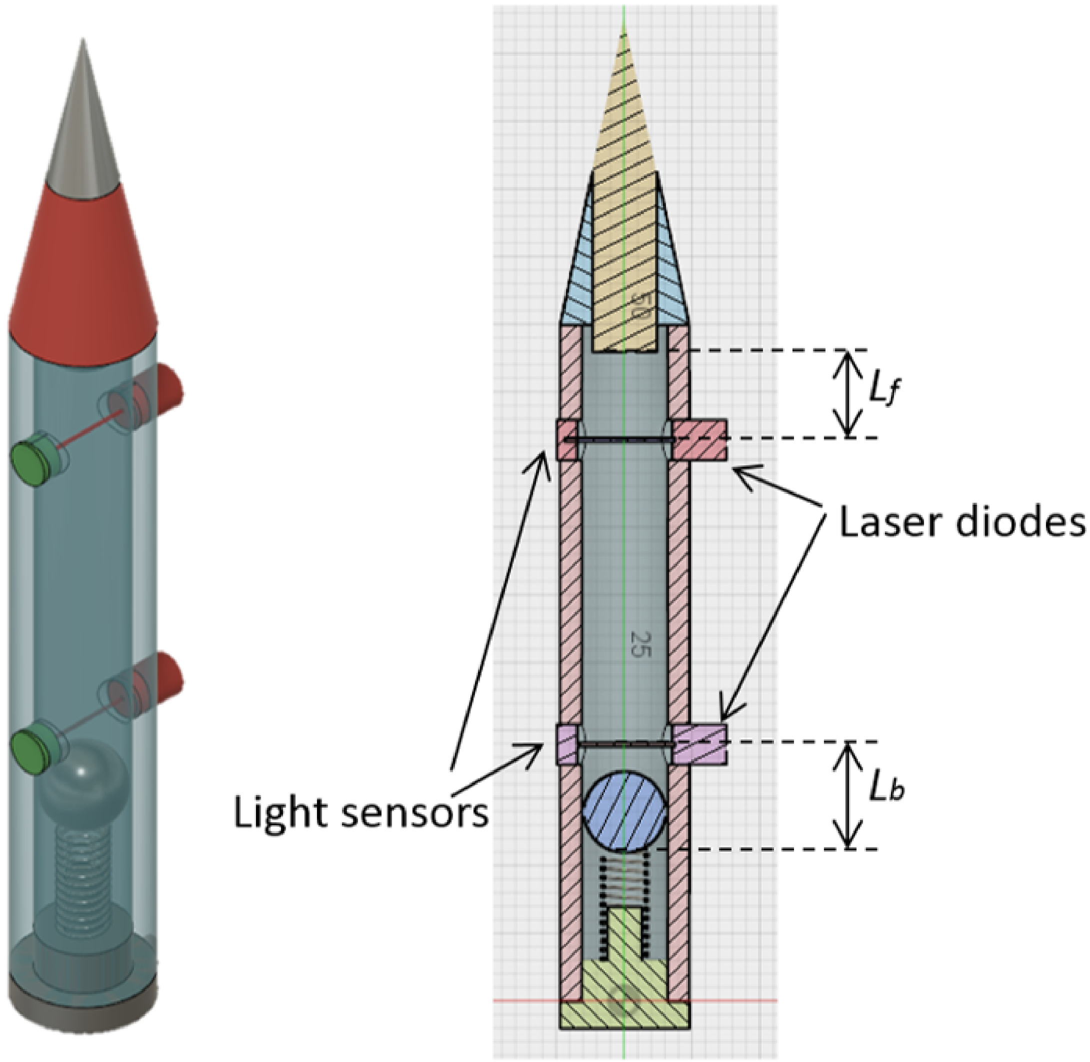

Figure 5.4: Magnetic hammer millirobot with laser diode-receiver pairs for measuring velocity, mounted at both ends.

5.3 Sphere motion sensing

5.3.1 Partial positioning and velocity measurement using lasers

Two laser diodes and two light sensors enable measuring the velocity of the sphere at each side of the MRbot (see fig. 5.4). When moving, the sphere interrupts the laser beam during a time t_i inversely proportional to the sphere's velocity v_s. By measuring t_i one can calculate the velocity v_s of the sphere with $v_s = 2 \cdot r_s/t_i$ where

r_s the sphere radius.

L_b is the distance between the posterior laser beam and the spring when not compressed. L_f is the distance between the anterior beam and the impact plate. The sphere must have enough space on both sides to completely cross the beam. This implies that $L_s > 2r_s$ and $L_b > 2 \cdot r_s - S_c$ with S_c being the maximum spring compression.

When the sphere moves toward the impact plate, it will interrupt the anterior laser beam during a time t_i and release it before the impact. It will then change direction and interrupt the anterior beam again. One can conclude that the sphere impacts the plate between the two interruptions of the laser beam. If L_s is close to $2r_s$ the interruption time will be short and the impact of the sphere can be detected by monitoring the signal of the anterior light sensor.

This method has been implemented on LabVIEW and a cRIO controller from National Instrument to detect the impact and change the field gradient direction to switch the direction of the force applied on the sphere after impact. At the same time, the velocity of the sphere is calculated before and after impact by measuring the interruption time t_i.

5.4 Complete position sensing using a vector of Hall effect probes

5.4.1 Method presentation

The ultimate goal of this method is to locate a magnetized ferromagnetic sphere in space, in 3D, using non-contact Hall effect sensors. We are here making a preliminary step in the study by searching to locate a magnetic sphere moving in one dimension.

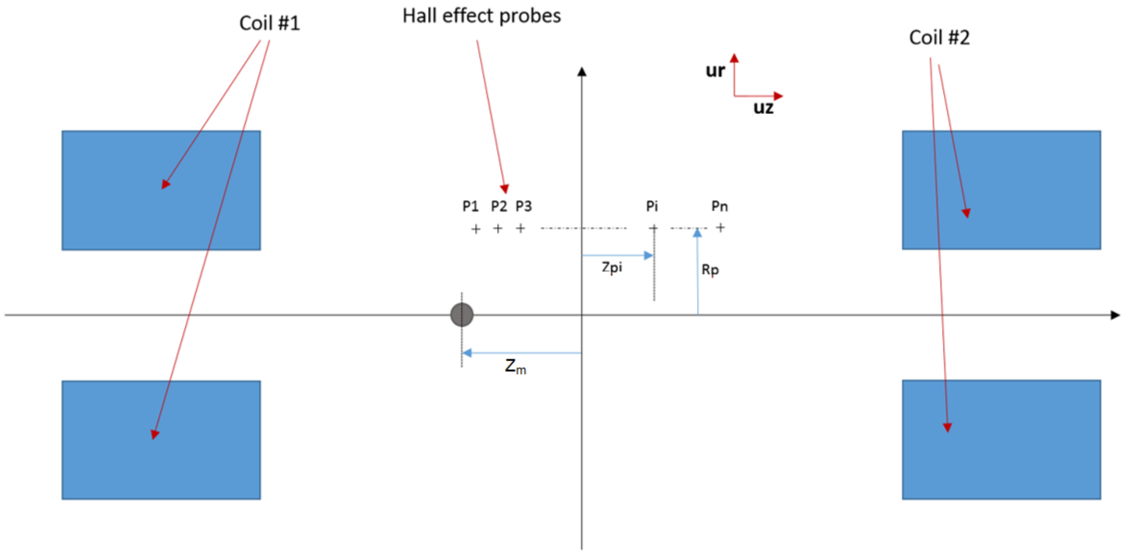

Figure 5.5: Representation of the magnetic system geometry

The ferromagnetic sphere is magnetized by solenoid coils producing a magnetic field. The magnetization of the sphere directly depends on the current in the coils as well as the position of the sphere. The magnetization of the sphere must be computed for each combination of position and electric currents.

5.4.2 Magnetic system configuration

The system is composed of two coils, a ferromagnetic sphere and a row of Hall effect probes. The two coils are collinear and their axes correspond to the z-axis of a cylindrical coordinate system (see fig. 5.5). The sphere is assumed to be at $r = 0$ and at $z = Z_m$ position (Z_m is the unknown of the problem). The row of Hall effect probes is oriented along the z-axis at radius distance $r = R_p$. The Hall effect probes only measure the radial component of the flux density.

5.4.3 Magnetic calculations

In this section the forward problem is solved, i.e. knowing the position Z_m, the magnetic flux density seen by the probes is calculated. The problem is inverted in a second step.

To calculate the flux density seen by the probes, the magnetization of the ferromagnetic sphere is calculated. The method used to calculate this magnetization is presented in Chapter 3.

To calculate the flux density produced by a sphere having a magnetization $\mathbf{M}$, it will be assumed that the radius of the sphere is sufficiently small to be modeled by a magnetic dipole $\mathbf{m}$. In addition, it will be assumed that the magnetization of the sphere is uniform. Hence, $\mathbf{m}$ is given by

$$\mathbf{m} = \iiint_{SphereVolume} \mathbf{M} \cdot dV. \tag{5.1}$$

The potential magnetic vector produced by the magnetic dipole situated on $r = 0$ and $z = Z_m$ on a calculation point Pi situated on $r = R_p$ and $z = Z_{pi}$, as explained in [24], is given by

$$\mathbf{A} = \frac{\mu_0}{4\pi} \frac{\mathbf{M} \times \mathbf{T}}{\|\mathbf{T}\|^3}, \tag{5.2}$$

where $\mathbf{T}$ is given by

$$\mathbf{T} = \begin{bmatrix} R_p \\ 0 \\ Z_m - Z_{pi} \end{bmatrix}. \tag{5.3}$$

The magnetic flux can be expressed as

$$\mathbf{B} = \nabla \times \mathbf{A}, \tag{5.4}$$

and the radial component of the flux density produced by the sphere at the point Pi

can be expressed as

$$B_r(Z_m, Z_{pi}) = \frac{3\mu_0 \left\|\mathbf{m}\right\| R_p \left(Z_m - Z_{pi}\right)}{4\pi \left(\left(Z_m - Z_{pi}\right)^2 + Rp^2\right)^{\frac{5}{2}}}. \tag{5.5}$$

5.4.4 Verification of the field calculation

The flux density obtained by using eq. 5.5 is compared here to the flux density calculated by a 2D axisymmetric finite element method with the software FEMM. The considered system is composed of two field coils each having an external radius of 46 mm, an internal radius of 13 mm and a length of 65 mm. Their center is separated by a distance d=119 mm. The sphere has a relative permeability μ_r=1000 and a radius equal to 1.59 mm. The Hall effect probes are placed at a radius R_p=5mm. The coils carry a current equal to 15 A and oriented in opposite directions.

Equation 5.5 corresponds to the field produced by the sphere only, when submitted to the field produced by the two coils. To obtain that with FEMM, two simulations need to be performed: one with the magnetic sphere and one without. The flux density produced by the sphere B_{sphere} is obtained by subtracting the flux density produced by the coils only B_{coils} from the flux density produced by the complete system B_{tot} (see figure 5.6). Figure 5.7 shows that that the flux density calculated using eq. 5.5 is close to the flux density obtained with FEMM. This validates the calculation method including the two assumptions made in part 5.4.3.

5.4.5 Measuring the field produced by the magnetic sphere only

The equations describing the forward problem have been presented. We now must invert the problem, i.e. calculate Z_m from the field measured on the Hall effect probes.

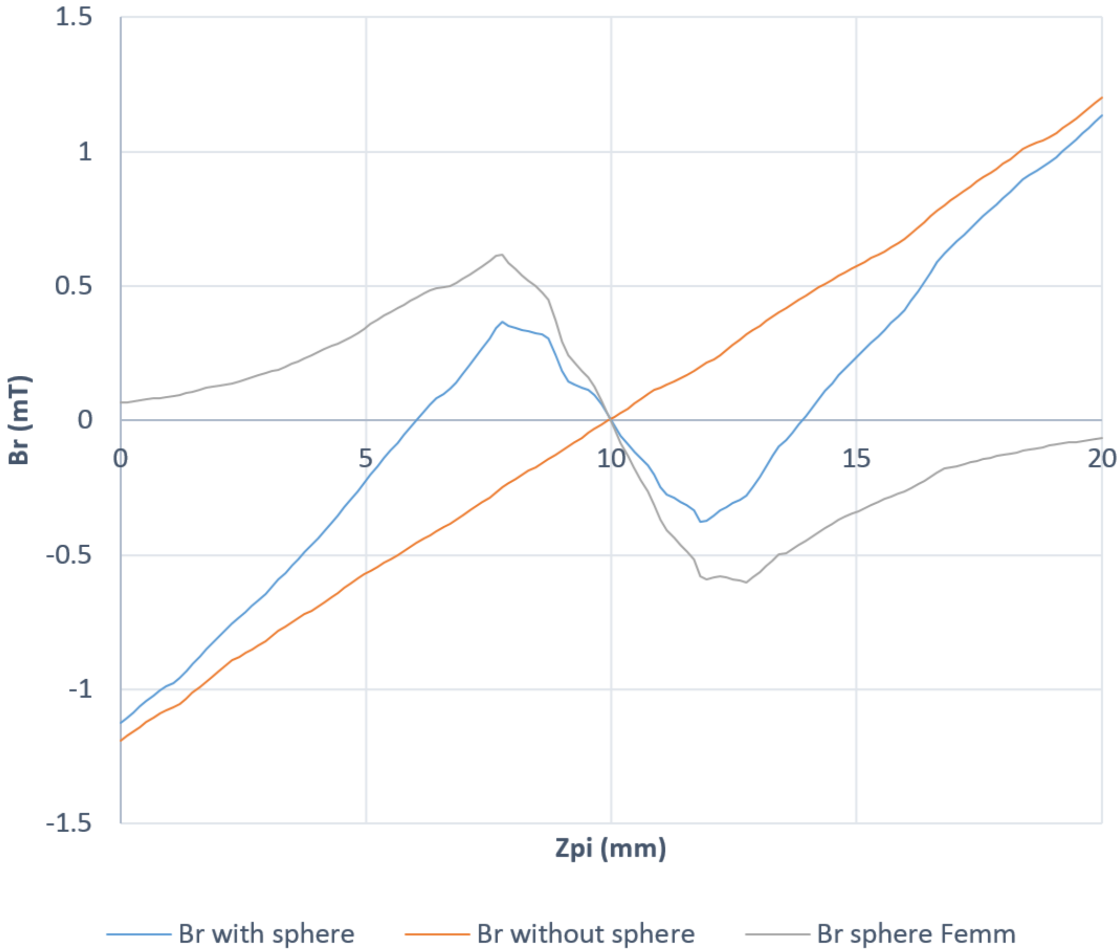

Figure 5.6: Magnetic flux density computed with FEMM (finite elements software). The orange curve is the result of the computation without a sphere. The blue curve is the result of the computation with the sphere. The grey curve is the difference between the two first curves. It correspond to the magnetic flux density produced by the sphere only.

First, the position Z_m is calculated from the flux density produced by the sphere only. However, the sensors are placed in the full system which includes the two field coils. The flux density measured by the sensors is the sum of the flux density produced by the coils and the spheres. We can in practice easily obtain the field produced by the spheres only by using the same technique used to plot figure 1: B_{coils} must be subtracted from B_{tot} to obtain B_{sphere}. This requires knowing the value of B_{coils}.

In an experimental setup, we can measure the current in each coil. We have a magnetic model that allows us to calculate B_{coils}. However, this would give a

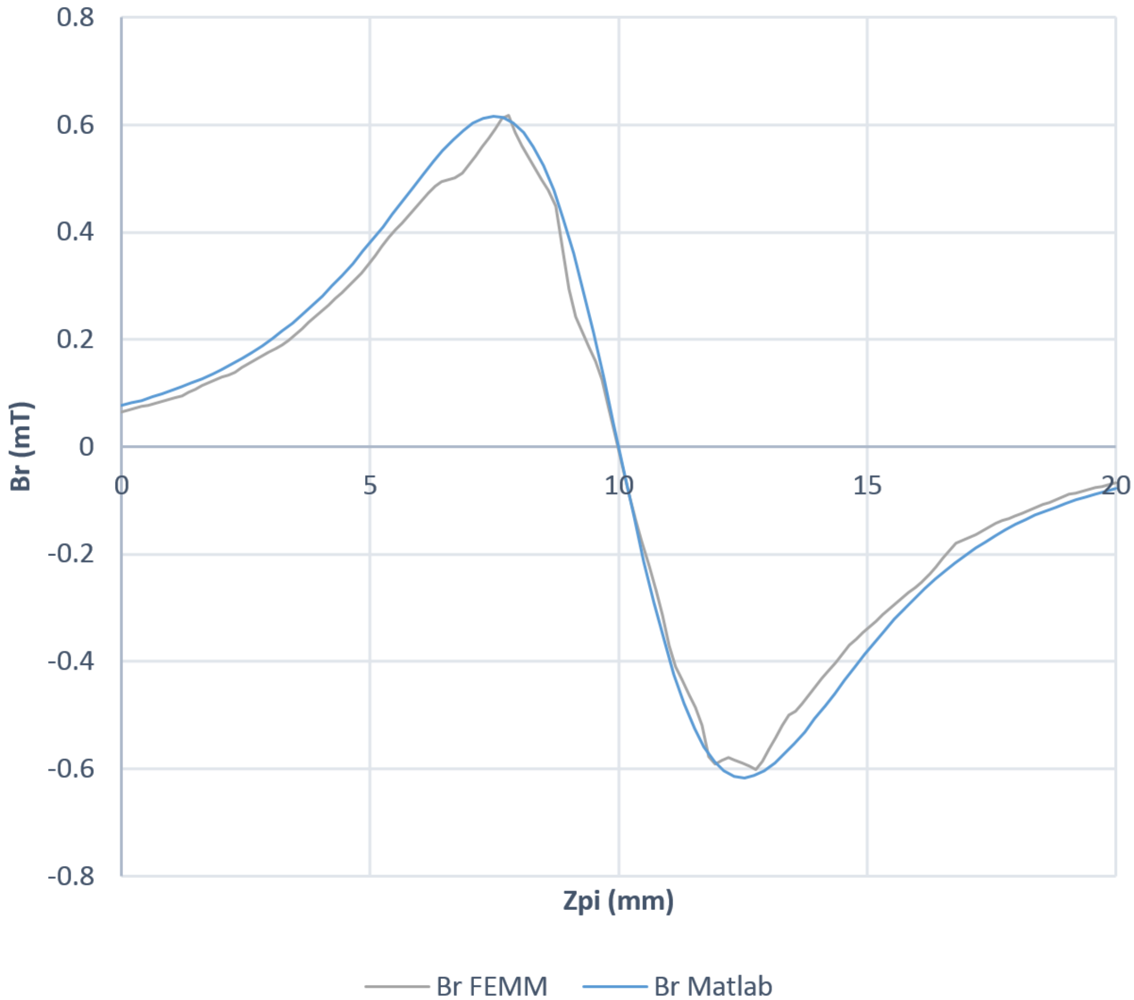

Figure 5.7: Magnetic flux density produced by the magnetic sphere. Comparison of the results obtained with FEMM and the calculation using eq. 5.5 implemented in MATLAB.

poor accuracy because our model assumes a perfect coil (coil with a uniform current density). The real coil is made of turns placed more or less accurately during the manufacturing process.

This problem can easily be overcome. The Hall effect sensors are mounted in a permanent place in the magnetic setup. The field produced by each coil on the sensors is directly measured on the experimental setup. B_{coils} is directly proportional to the current in the coil. We can therefore, for each sensor and each coil, experimentally find the coefficient that relates B_{coil} and the current. This will give a high accuracy in the calculation of B_{coils}.

Remark: The Hall effect probes only measure the radial component of the flux density in this setup. This component was chosen rather the axial one because the flux density produced by the coils are mainly axial. The ratio between the flux density produced by the sphere and the flux density produced by the coils is larger on the radial component. It is more accurate to measure the radial component of the field and calculate B_{sphere} from it.

5.4.6 Calculation of the position

Inverse problems are sensitive to measurement noise (a small error on the measurement will produce a large error on the calculated position). Adding more Hall effect sensors to have an overdetermined system improves the estimate.

In the following, $B_{rm}(i)$ will correspond to the radial flux density measured by a Hall sensor situated on $z = Z_{pi}$ and $r = R_p$. The vector containing all measured $B_{rm}(i)$ is noted $\mathbf{B_{rm}}$.

The position Z_m is calculated by performing a least square non-linear regression. The optimization algorithm used is a simple gradient descent.

The measured flux density is fitted by equation 5.5. Z_m is the unknown of the system. The objective function to minimize is given by

$$obj(Z_m) = \sum_{i=1}^{n} \left(B_r(Z_m, Z_{pi}) - B_{rm}(i)\right)^2. \tag{5.6}$$

The starting point of the optimization Z_{m0} is a rough evaluation of the solution. It is equal to the average of the position Z_{pi} of the sensors that give the maximum and minimum value for B_{rm}. The flux density value crosses the abscissa axis at approximately $Z = Z_m$. Thus the solution must be somewhere around the middle of the point giving the maximum field and the minimum field. Hence Z_{m0} can be evaluated as

$$Z_{m0} = \frac{Z_{Bmax} + Z_{Bmin}}{2}. \tag{5.7}$$

Here Z_{Bmax} and Z_{Bmin} are the z position of the Hall sensors giving the maximum and minimum flux density.

5.4.7 Theoretical tests of the method

Properly testing the method requires studying the effect of the measurement incertitude (measurement noise) on the found position. A Monte Carlo method was used. The different steps are:

1. A problem geometry is chosen (number of probes, distance between probes, radius, etc.).
2. A random position Z_{mObj} is generated.
3. The magnetic flux density on the Hall effect probes is calculated using eq. 5.5.
4. A measurement noise level (NL) is chosen (it can be manually selected or randomly generated).
5. A measurement noise is added with a *rand()* function to the previously calculated magnetic flux density. For each sensor, a noise voltage selected uniformly at random between $-NL$ and NL is added to $B_{rm}(i)$. The obtained values represents the measurements obtained via the Hall effect sensors $B_{rm}(i)$.
6. The position of the sphere is calculated from B_{rm}. The position found (noted Z_{mFound}) is compared to the actual position Z_{mObj} and the error can be calculated.
7. Return to step 2 and perform as many loops as needed to have consistent statistical data.

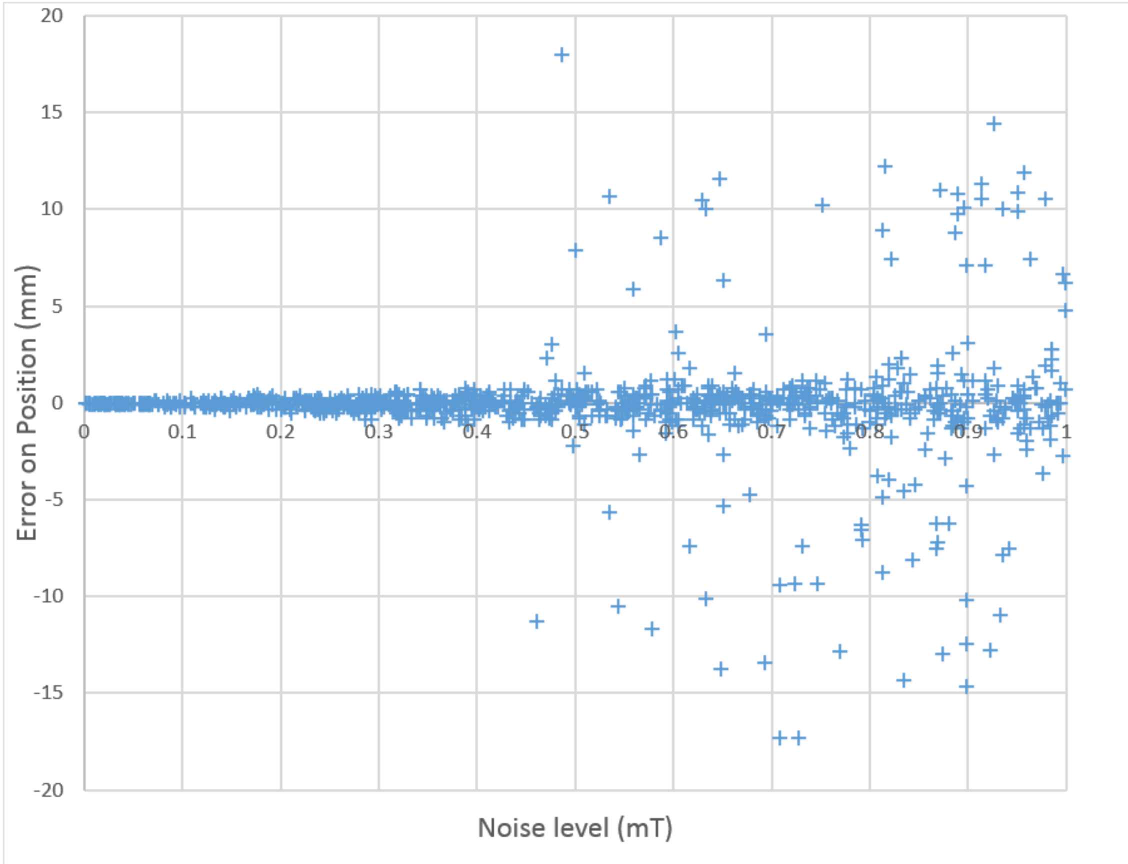

Figure 5.8: Error on Z_{mFound} as a function of the noise level NL.

All the results of simulations shown later correspond to the system simulated in Section 5.4.4 with $Z_m \in [-10\text{mm}, 10\text{mm}]$.

5.4.8 Effect of measurement noise

1000 data points were generated with the following parameters: 20 probes placed between -15 and +15 mm, 3 iterations of the gradient descent optimization. For each point, the noise level NL was generated randomly. Figure 5.8 shows a plot of the error on the position found $(Z_{mFound} - Z_{mObj})$ as a function of NL.

In this case, the maximum tolerable NL is 0.45 mT. Under this noise level, the positioning is accurate enough to locate the sphere at plus or minus 1 mm approximately. Above this value, large positioning errors are encountered on some of the

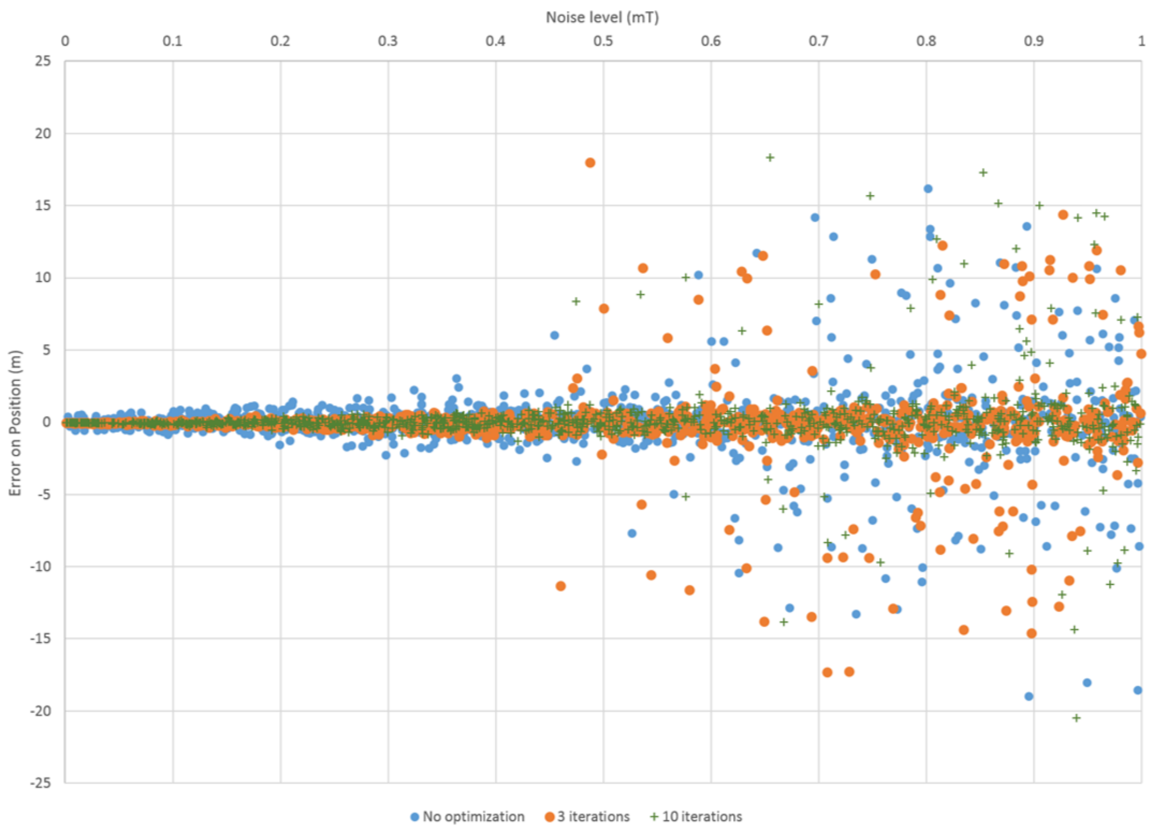

Figure 5.9: Error on Z_{mFound} as a function of the noise level NL for three optimization configurations

data points.

5.4.9 Effect of number of iterations in gradient descent

Figure 5 shows the error $(Z_{mFound} - Z_{mObj})$ as a function of NL for different optimization configuration. Results show that the initial point Z_{m0} is already very close to the solution. The gradient descent optimization slightly improves accuracy. Three iterations are sufficient to reach the maximum accuracy.

5.4.10 Effect of the radial position Rp

Figure 5.10 is a plot of the error on the found position $(Z_{mFound} - Z_{mObj})$ as a function of NL for two different radial position of the Hall effect sensors. Result

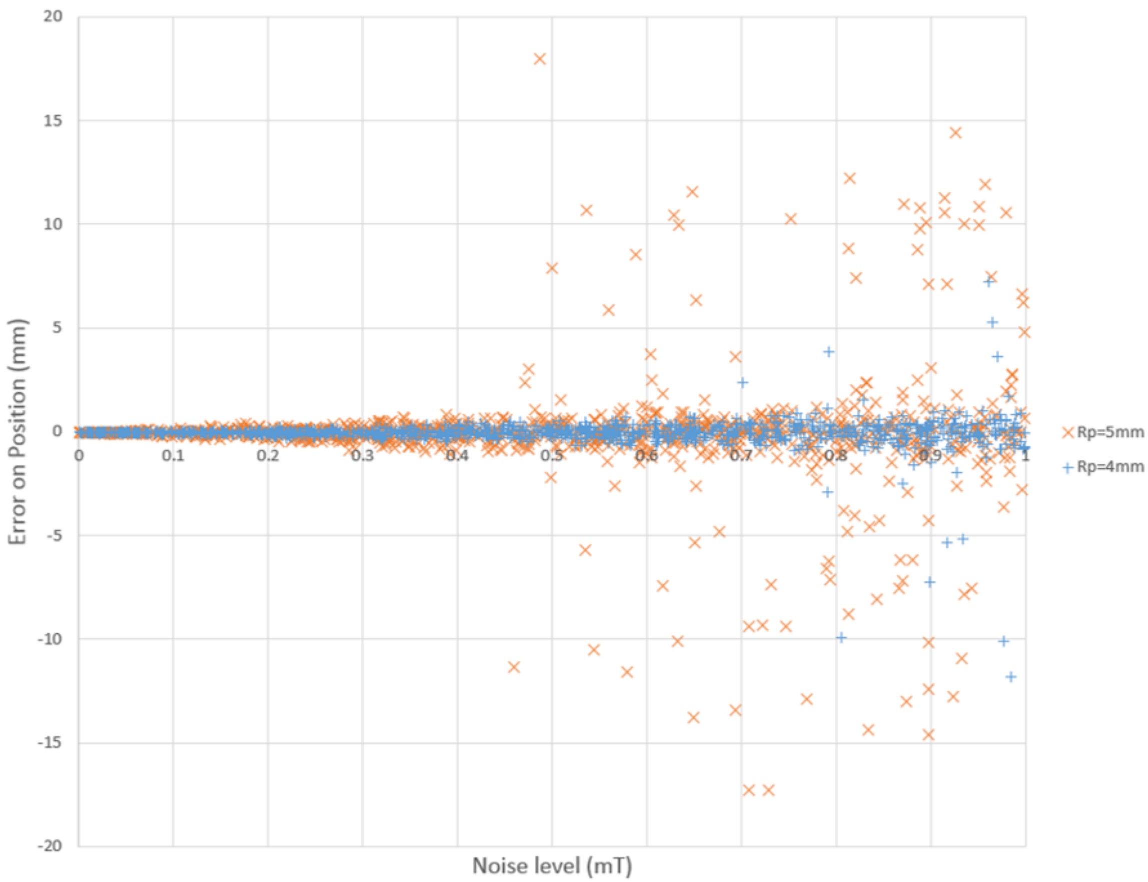

Figure 5.10: Error on Z_{mFound} as a function of the noise level NL for two radial positions of the Hall effect sensors.

accuracy increases if the sensors are closer to the sphere because signal strength increases with proximity.

5.4.11 Effect of the number of probes

The number of probes has a large effect on the accuracy of the method. On Fig. 5.11 and 5.12, the objective function (see eq. 5.6) of the optimization is plotted as a function of Z_m. Figure 5.11 is plotted for NL=0 T and fig. 5.12 for NL=0.001 T.

On Fig. 5.11 the position of the sphere correspond to the minimum of the function. When the number of probes increases, the gradient of the objective function

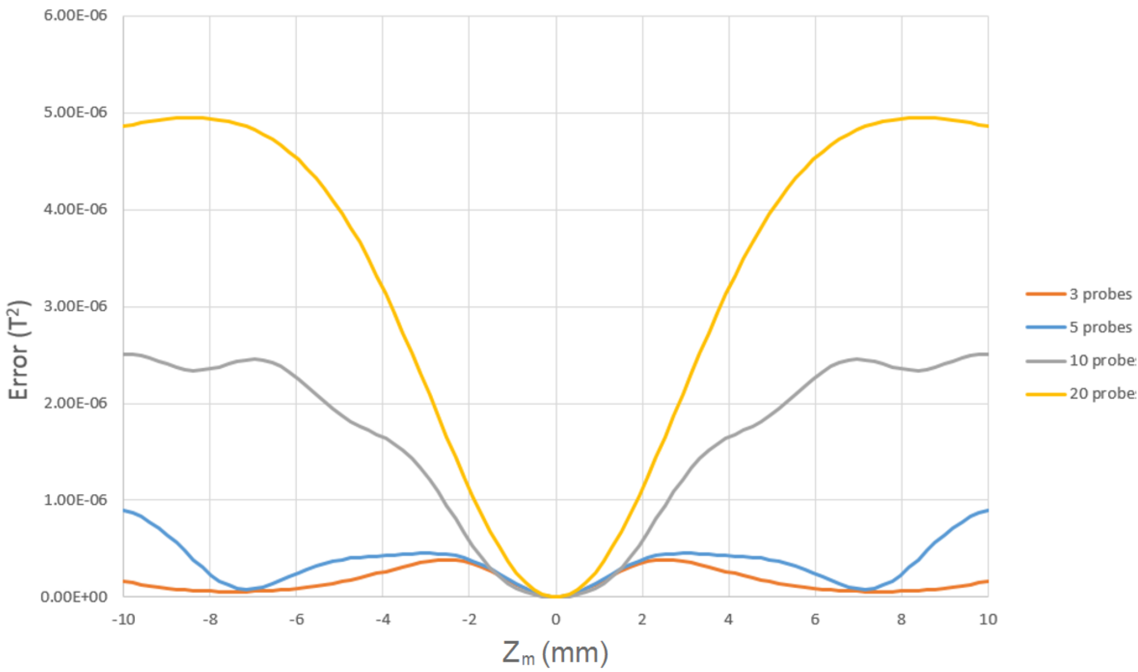

Figure 5.11: Objective function as a function of Z_m for different numbers of Hall effect probes with NL=0 T.

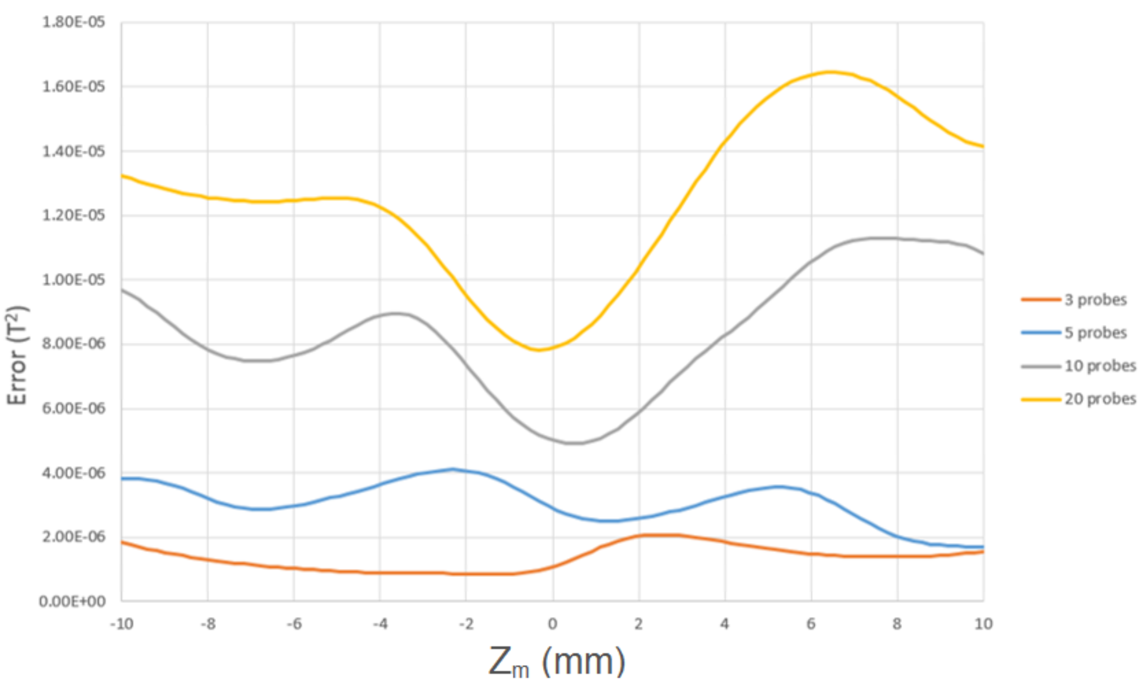

Figure 5.12: Objective function as a function of Z_m for different number of Hall effect probes.

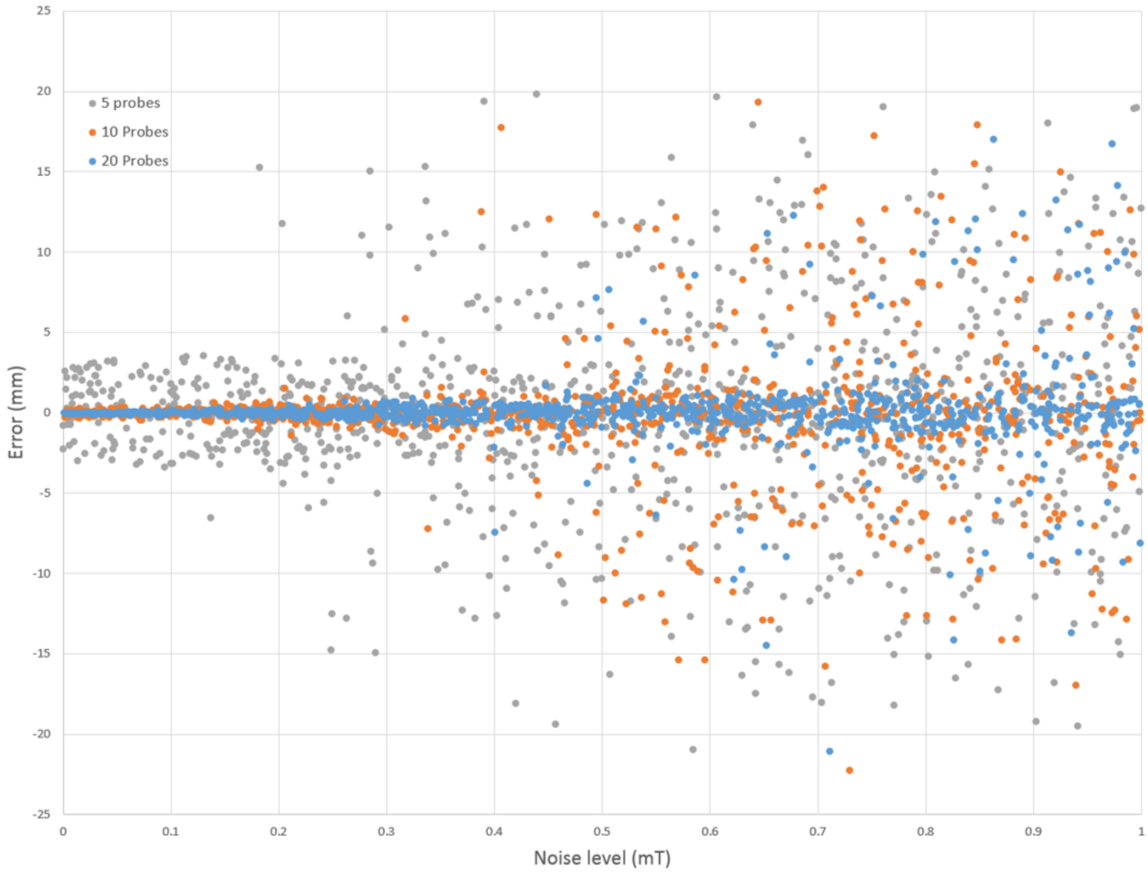

Figure 5.13: Error on Z_{mFound} as a function of the noise level NL with 5, 10 and 20 Hall effect sensors.

increases, making the search of the minimum of the function easier. Also, in the calculation area (-10 mm, + 10 mm), the function for 3-5 and 10 probes have local minimums. This is a concern when performing optimizations because there is a risk that the algorithm will return a local minimum. When the number of probes increases, the local minimums become less pronounced.

Figure 5.13 shows that the measurement noise changes the shape of the objective function. First, the minimum of the function is slightly changed. This corresponds to the inevitable error on the calculated position when there is a measurement error. In this case, the local minimums are more pronounced. Again, on this plot, the more probes that are present, the less pronounced are the global minimums and the steeper is the gradient. This makes determining the position both easier and more

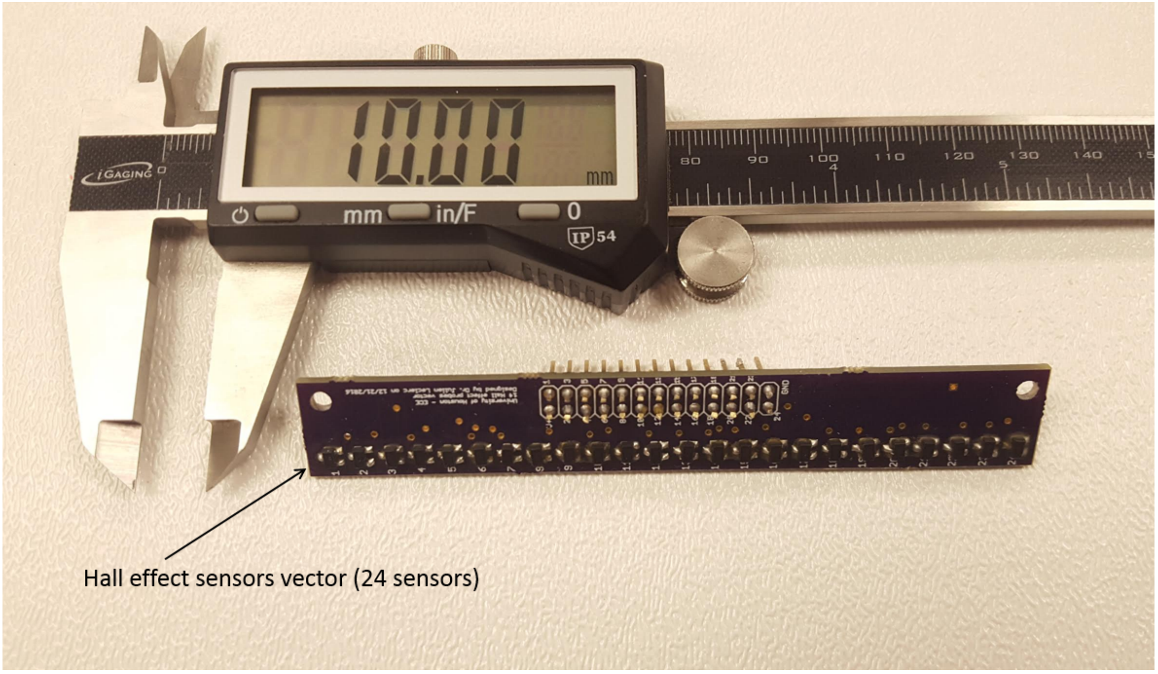

Figure 5.14: PCB board with a vector of 24 Hall effect sensors.

accurate. Remark: On Fig. 5.8 (for example) the error stays low at low noise level but suddenly, when the noise increases, some points Z_{mFound} have large errors. This probably corresponds to points where the conjugate gradient converged toward a local minimum.

Figure 5.13 shows a plot of the error on Z_{mFound} as a function of NL for 5, 10 and 20 probes. As expected, larger the numbers of probes result in more accurate positioning of the probe. For example, for this configuration, using only 5 probes is not acceptable.

5.4.12 Practical realization

A Hall effect probe array containing 24 probes was built (Figure 5.14). The device has not been tested on a practical experiment yet. It will be tested soon.

5.5 Partially closed loop experiment

The coils are driven by square shaped current waveform. The current in the coils can either be I_{max} or 0 A. The coil will be said to be "on" when $I = I_{max}$ and "off" when $I = 0$ A.

As explained in Chapter 4, the magnetic hammer generates maximum impact velocities when the input gradient force is always in the same direction as the motion of the sphere. This is equivalent to an ideally closed-loop system. An open-loop control is inefficient, as shown in Fig. 4.3. The force applied on the sphere (and therefore the magnetic gradient) must change direction when the sphere hits the impact plate and when the sphere changes direction on the spring side to provide maximum impulse.

Our eventual goal is to use these robots in an MRI scanner, where MRI gradients must be shared for propulsion and position feedback [17]. The nature of our system enables simpler sensing requirements that can be accomplished with a simple microphone. The microphone is used to monitor the noise produced by the system. The impact noise creates a larger pulsed signal on the microphone output and can, therefore, be easily detected. When the impact is detected, the anterior coil is turned off while the posterior coil is turned on. The force applied on the sphere now pushes it backward, toward the spring side.

The current stays constant during a time t_s after the impact is detected. The anterior coil is subsequently turned on, and the posterior coil is turned off. The force then pushes the sphere forward. The current in the coils is changed again when another impact is detected. This process is repeated indefinitely.

t_s is manually tuned while the system is working. It is set to the value that gives the maximum oscillating frequency. This value corresponds to a gradient that changes direction when the sphere velocity is zero on the spring side. It should give the same results as the perfectly closed-loop simulations.

The partially closed-loop experiment was performed and compared to the model. Figure 5.15 shows a comparison of the optimum oscillating frequency as a function of I_{max}. When I_{max} increases, the oscillating frequency increases. The force on the sphere increases with I_{max} and consequently increases the moving speed of the sphere. This figure also shows that the model without friction has the same slope as the experimental data. However, the simulation signals are approximately 1 Hz faster than the experiment. This difference probably comes from the lack of friction in the model. The next subsection adds the effect of friction to the model.

5.5.1 Effect of friction

To improve the model accuracy, the friction between the moving sphere and the other components of the millirobot was included into the model. The sphere can be rolling or sliding inside the tube. The modelization is based on the method described in [25]. The rotation speed $\dot{\theta}$ is first computed and drag is calculated from this result.

The friction on the tube produces a torque on the sphere. It is assumed that the coefficient of static friction is equal to the coefficient of kinetic friction μ_k. The equation used to calculate the angular velocity variation $\frac{\mathrm{d}\dot{\theta}}{\mathrm{d}t}$ of the sphere is different whether the sphere is rolling or sliding. The distinction between these two different behaviors is made by calculating the relative velocity, V_{rel}, between the sphere and the tube surface. This is given by eqn. (5.8) as

$$V_{rel} = V - r\dot{\theta}. \tag{5.8}$$

If the relative speed is inferior to 0.005 m/s and if the force applied to the sphere is smaller than the kinetic friction, the sphere is considered to be rolling inside the tube

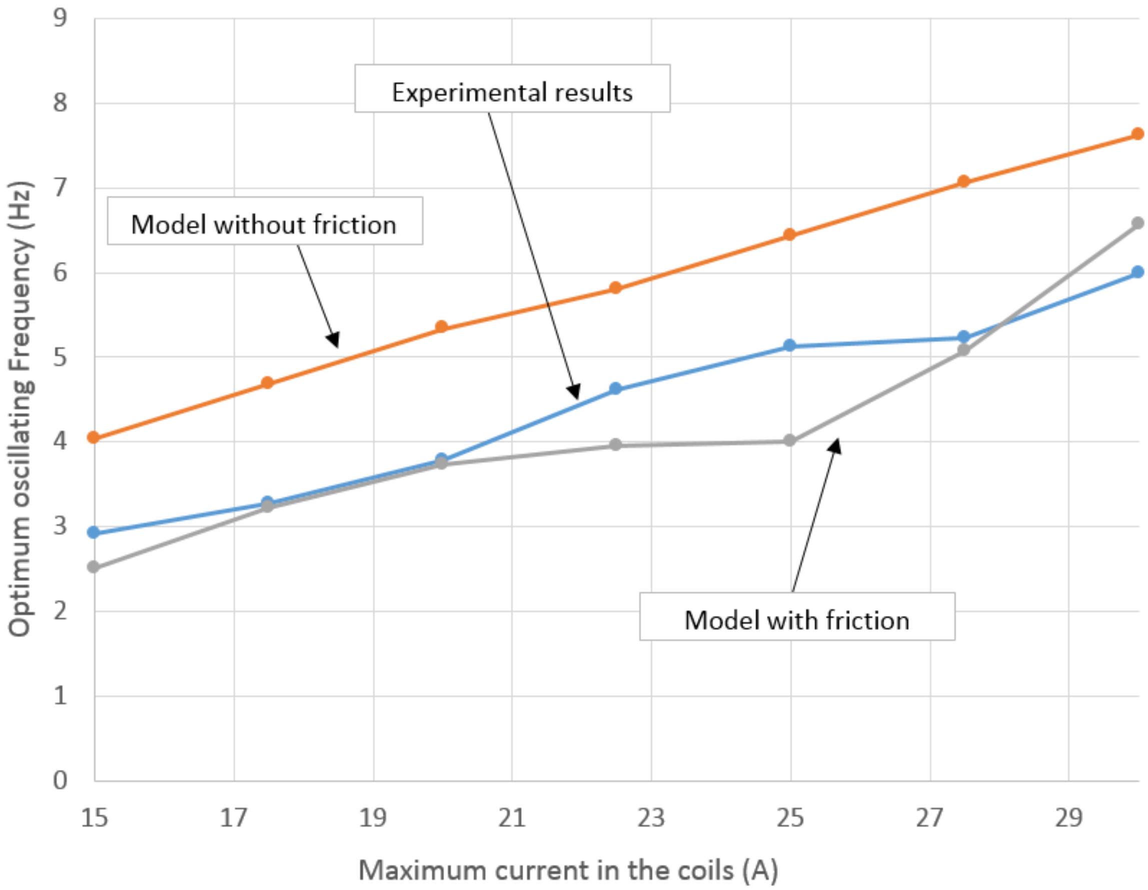

Figure 5.15: Comparison between the oscillating frequency obtained experimentally and with the model as a function of the current in the coils I_{max}.

and the drag is null. $\frac{\mathrm{d}\dot{\theta}}{\mathrm{d}t}$ can be calculated from

$$\frac{\mathrm{d}\dot{\theta}}{\mathrm{d}t} = r\frac{\mathrm{dV}}{\mathrm{d}t}. \tag{5.9}$$

In all other cases, the torque applied to the sphere is equal to the kinetic friction force multiplied by the sphere radius. The drag is equal to the kinetic friction force $\mu_k = 0.2$.

Results of simulations are shown in Fig. 5.15. The addition of the friction greatly improves the model accuracy.

Chapter 6

Conclusion

A magnetic hammer system for a millirobot driven by the gradient fields of an MRI scanner was studied. The system enables producing the forces large enough to penetrate body tissue. The hammer is composed of a ferromagnetic sphere moving inside a tube. On the posterior side of the robot, there is a spring that allows changing the direction of the sphere smoothly. On the anterior side, a hard metal rod act as an impact plate to transfer the momentum of the ferromagnetic sphere to the body of the robot. The system is driven by an external magnetic field, such as that produced by an MRI scanner. The main field magnetizes the sphere and the gradient produces the forces necessary to move the sphere.

A model allows the computation of the position of the sphere as a function of time. The magnetic flux density and the gradient are computed using a semi-analytical method and allow an accurate calculation of the force applied to the sphere.

The coefficients of restitution for different impact rod materials and diameters were determined experimentally. These measurements showed that titanium impact rods exhibit the largest values of e for diameters of $\frac{1}{8}$" and $\frac{1}{4}$". Aluminum exhibited the highest value of e among $\frac{3}{16}$" diameter rods. The visible indentation of the Aluminum impact surface for this diameter could be a reason for the spike in the magnitude of e. Both titanium and aluminum are lightweight, a useful property to achieve neutral buoyancy of millirobots. Bio-compatibility of these materials will be verified in further studies.

Ideally closed-loop, partially closed-loop and open-loop control strategies are compared numerically, analytically and experimentally. A desktop-size magnetic test bench was built to reduce experimental cost related to the use of a clinical MRI scanner. An ideal closed-loop system generates the maximum average impact velocity over n impacts. A partially closed-loop system can be tuned to achieve ideally closed-loop values of average impact velocity for low values of friction. Open-loop systems generate the lowest values of average impact velocity.

Different sensing methods were used to experimentally test the control strategies. A microphone sensor was used with a laser diode-receiver pair to track the motion of the sphere at both ends of the millirobot. This was used to implement the partially and ideally closed-loop systems. Experimental results were found to validate our analytical and numerical models.

In future work, the control of the magnetic hammer will be implemented and tested in a clinical MRI scanner. The impact will be detected with the MRI signal instead of a microphone. The tradeoffs involved in miniaturization of the robot will also be studied.

References

[1] M. Sitti, H. Ceylan, W. Hu, J. Giltinan, M. Turan, S. Yim, and E. Diller, "Biomedical Applications of Untethered Mobile Milli/Microrobots," *Proceedings of the IEEE*, vol. 103, no. 2, pp. 205–224, Feb 2015.

[2] A. Vikram Singh and M. Sitti, "Targeted Drug Delivery and Imaging Using Mobile Milli - Microrobots: A Promising Future Towards Theranostic Pharmaceutical Design," *Current pharmaceutical design*, vol. 22, no. 11, pp. 1418–1428, 2016.

[3] S. Firebaugh, J. Piepmeier, E. Leckie, and J. Burkhardt, "Jitterbot: A Mobile Millirobot Using Vibration Actuation," *Micromachines*, vol. 2, no. 2, pp. 295–305, 2011. [Online]. Available: http://www.mdpi.com/2072-666X/2/2/295

[4] J.-B. Mathieu, G. Beaudoin, and S. Martel, "Method of Propulsion of a Ferromagnetic Core in the Cardiovascular System through Magnetic Gradients Generated by an MRI System," *IEEE Transactions on Biomedical Engineering*, vol. 53, no. 2, pp. 292–299, 2006.

[5] R. H. Taylor, *Computer-integrated Surgery: Technology and Clinical Applications*. Mit Press, 1996.

[6] A. Chanu, O. Felfoul, G. Beaudoin, and S. Martel, "Adapting the Clinical MRI Software Environment for Real-time Navigation of an Endovascular Untethered Ferromagnetic Bead for Future Endovascular Interventions," *Magnetic Resonance in Medicine*, vol. 59, no. 6, pp. 1287–1297, 2008. [Online]. Available: http://dx.doi.org/10.1002/mrm.21638

[7] S. Martel, J.-B. Mathieu, O. Felfoul, A. Chanu, E. Aboussouan, S. Tamaz, P. Pouponneau, L. Yahia, G. Beaudoin, G. Soulez, and M. Mankiewicz, "Automatic Navigation of an Untethered Device in the Artery of a Living Animal Using a Conventional Clinical Magnetic Resonance Imaging System," *Applied physics letters*, vol. 90, no. 11, p. 114105, 2007.

[8] A. T. Becker, O. Felfoul, and P. E. Dupont, "Toward Tissue Penetration by MRI-powered Millirobots Using a Self-assembled Gauss Gun," in *2015 IEEE International Conference on Robotics and Automation (ICRA)*, May 2015, pp. 1184–1189.

[9] T. Honda, K. Arai, and K. Ishiyama, "Micro Swimming Mechanisms Propelled by External Magnetic Fields," *IEEE Transactions on Magnetics*, vol. 32, no. 5, pp. 5085–5087, 1996.

[10] M. Sendoh, K. Ishiyama, and K. I. Arai, "Direction and Individual Control of Magnetic Micromachine," *IEEE transactions on magnetics*, vol. 38, no. 5, pp. 3356–3358, 2002.

[11] M. Sendoh, K. Ishiyama, K. I. Arai, M. Jojo, F. Sato, and H. Matsuki, "Fabrication of Magnetic Micromachine for Local Hyperthermia," *IEEE transactions on magnetics*, vol. 38, no. 5, pp. 3359–3361, 2002.

[12] F. Sato, M. Jojo, H. Matsuki, T. Sato, M. Sendoh, K. Ishiyama, and K. I. Arai, "The Operation of a Magnetic Micromachine for Hyperthermia and its Exothermic Characteristic," *IEEE transactions on magnetics*, vol. 38, no. 5, pp. 3362–3364, 2002.

[13] R. Dreyfus, J. Baudry, M. L. Roper, M. Fermigier, H. A. Stone, and J. Bibette, "Microscopic Artificial Swimmers," *Nature*, vol. 437, no. 7060, pp. 862–865, 2005.

[14] J. J. Abbott, K. E. Peyer, M. C. Lagomarsino, L. Zhang, L. Dong, I. K. Kaliakatsos, and B. J. Nelson, "How Should Microrobots Swim?" *The international journal of Robotics Research*, vol. 28, no. 11-12, pp. 1434–1447, 2009.

[15] S. Martel, J.-B. Mathieu, O. Felfoul, H. Macicior, G. Beaudoin, G. Soulez, and L. Yahia, "Adapting MRI Systems to Propel and Guide Microdevices in the Human Blood Circulatory System," in *Engineering in Medicine and Biology Society, 2004. IEMBS'04. 26th Annual International Conference of the IEEE*, vol. 1. IEEE, 2004, pp. 1044–1047.

[16] P. Pouponneau, G. Bringout, and S. Martel, "Therapeutic Magnetic Microcarriers Guided by Magnetic Resonance Navigation for Enhanced Liver Chemoembilization: A Design Review," *Annals of Biomedical Engineering*, vol. 42, no. 5, pp. 929–939, 2014. [Online]. Available: http://dx.doi.org/10.1007/s10439-014-0972-1

[17] O. Felfoul, A. T. Becker, G. Fagogenis, and P. E. Dupont, "Simultaneous Steering and Imaging of Magnetic Particles Using MRI Toward Delivery of Therapeutics," *Scientific Reports*, vol. 6, 2016.

[18] C. Simone and A. M. Okamura, "Modeling of Nedle Insertion Forces for Robot-assisted Percutaneous Therapy," in *Robotics and Automation, 2002. Proceedings. ICRA'02. IEEE International Conference on*, vol. 2. IEEE, 2002, pp. 2085–2091.

[19] A. M. Okamura, C. Simone, and M. D. O'leary, "Force Modeling for Needle Insertion into Soft Tissue," *IEEE transactions on biomedical engineering*, vol. 51, no. 10, pp. 1707–1716, 2004.

[20] M. Mahvash and P. E. Dupont, "Mechanics of Dynamic Needle Insertion into a Biological Material," *IEEE Transactions on Biomedical Engineering*, vol. 57, no. 4, pp. 934–943, 2010.

[21] S. Hidalgo-Tobon, “Theory of Gradient Coil Design Methods for Magnetic Resonance Imaging,” *Concepts in Magnetic Resonance Part A*, vol. 36A, no. 4, pp. 223–242, 2010. [Online]. Available: http://dx.doi.org/10.1002/cmr.a.20163

[22] J. C. Simpson, J. E. Lane, C. D. Immer, and R. C. Youngquist, “Simple Analytic Expressions for the Magnetic Field of a Circular Current Loop,” *NASA Technical report*, 2001.

[23] F. E. M. Magnetics, “http://www.femm.info.”

[24] T. Chow, *Introduction to Electromagnetic Theory: A Modern Perspective.* Jones and Bartlett Publishers, 2006. [Online]. Available: https://books.google.com/books?id=dpnpMhw1zo8C

[25] J. Hierrezuelo and C. Carnero, “Sliding and Rolling: The Physics of a Rolling Ball,” *Physics Education*, vol. 30, no. 3, p. 177, 1995. [Online]. Available: http://stacks.iop.org/0031-9120/30/i=3/a=009